2009

Effect of Osteopontin and Related Peptides on Hydroxyapatite Crystallization Studied by Dynamic Light Scattering

Ron Dauphinee

Effect of Osteopontin and Related Peptides on Hydroxyapatite Crystallization Studied by Dynamic Light Scattering

(Spine title: Light Scattering Study of Hydroxyapatite Crystallization)

(Thesis Format: Monograph)

by

Ron Dauphinee

Faculty of Science
Department of Physics and Astronomy

A thesis submitted in partial fulfillment
of the requirements for the degree of
Master of Science

School of Graduate and Postdoctoral Studies
The University of Western Ontario
London, Ontario, Canada

Abstract

We investigate the use of dynamic light scattering for quantitatively assessing the effectiveness of certain bone-related proteins on the formation of hydroxyapatite crystals. Hydroxyapatite, $Ca_{10}(PO_4)_6(OH)_2$, is the major mineral component of virtually all calcified tissue within the body. It is also present in numerous pathological calcifications including kidney stones and arterial plaque. There are a number of established assays for studying the potencies of proteins that modulate mineral formation, but they generally provide limited and often only qualitative information. We use dynamic light scattering to measure the size and growth rate of crystals precipitating from a solution of calcium and phosphate ions in the presence of various proteins. The mineral-modulating effects of bone-derived osteopontin, recombinant osteopontin, synthetic poly-aspartic acid, and a 16-residue peptide derived from osteopontin (residues # 65-80, called pOPAR) are studied. From the intensity and the decay rate of the intensity autocorrelation function of the scattered light, we find that native osteopontin completely inhibits the nucleation of mineral crystals over the two-hour duration of the measurements. Poly aspartic acid and pOPAR are also effective inhibitors, though higher concentrations of these peptides are required to completely inhibit precipitation than for native osteopontin. In contrast, recombinant osteopontin does not affect crystal nucleation, but appears to effectively inhibit crystal growth. These results demonstrate the utility of dynamic light scattering in the assessment of the effects of proteins and peptides on mineral formation in real time.

Key Words: dynamic light scattering, osteopontin, crystal growth, nucleation, hydroxyapatite, protein-crystal interactions

Acknowledgements

First and foremost I would like to acknowledge my girlfriend Kate Ross for supporting me as I have worked my way through this degree. Your emotional support and positive attitude have proven invaluable, keeping me focused and motivated through the more difficult aspects of the research and writing processes. I love you Kate.

I would like to thank my two supervisors Dr. John de Bruyn and Dr. Harvey Goldberg. In particular I would like to thank John for taking me on as a student for this masters program, but you were both fantastic in your patience, guidance and advice as I worked my way through this project. I have enjoyed my time with you both.

I would also like to thank Dr. Graeme Hunter for his input and guidance on this project as well as Dr. Peter Simpson and Dr. William Lennard for their assistance, input an encouragement as my advisory committee members.

Additionally, I owe a great deal of thanks to my friends and colleagues, in particular, Paul Azzopardi, Gurpreet Baht, Aaron Langdon, Erik Holm, Krista Vincent, Vasek Pitelka and Jason O'Young. Your friendship and the adventures we have shared together, I will remember forever. From partying in Montreal and Niagra Falls, to surviving torrential rains in Algonquin, to curling and making wine, I have treasured my time with you all. I would also like to thank Felix Oppong, Simon de Vet, Peter Wright, Nan Yang, Dr. Bernd Grohe, Heidi Lao and Hong Chen. If it were not for the friendships we have formed, the guidance and the assistance I have received from all of you, this project would have been infinitely more difficult.

Finally, I would like to thank my family, and of course everyone else that I have had the pleasure of befriending here in London.

Contents

List of Tables

List of Figures

Chapter 1

Introduction

The ability of organisms to biologically control mineral formation for various purposes, including the development of skeletal and protective structures, is key to the survival of an immense array of lifeforms. Despite this, biomineralization remains poorly understood. The purpose of the research described in this thesis was to investigate the use of dynamic light scattering to measure the effect of various bone-related proteins on biomineralization. The first chapter of this thesis provides an introduction to biomineralization, crystal formation, the role of proteins in this process, and current methods of assessing the role of proteins in biomineralization. Chapters two and three describe the materials and methods used, first introducing light scattering in a broad sense, followed by a detailed discussion of dynamic light scattering and an explanation of the experimental setup used in the present work. The fourth and fifth chapters present the results of our experiments and discus their significance. The thesis ends with a brief summary of the results and a discussion of the potential of light scattering as an assay with biomineralization applications.

1.1 Biomineralization

Biomineralization is the process by which living organisms form minerals for their own requirements [1]. Over the last 550 million years, organisms from all five kingdoms have developed the capacity to synthesize over 64 different biominerals [2]. For example, mollusks construct shells made of argonite and calcite, two different forms of calcium carbonate, $CaCO_3$ [3]. Human bones and teeth consist principally of hydroxyapatite, $Ca_{10}(PO_4)_6(OH)_2$ [4], while some plants produce structures made of calcium oxalate (CaC_2O_4) that act both as internal calcium reservoirs and as a defense against herbivores [5].

Biominerals are often mineral-organic composites [1]. They are primarily mineral in their composition, but are often constructed in and around an organic lattice or mold that is incorporated into the structure. The organic matrix is specific for different structures, even within a single organism, and is generally responsible for providing flexibility and fracture resistance that are far superior to pure mineral equivalents [6]. As a result of this biological context, biominerals are generally formed under very regulated conditions [7,8]. This often results in materials that have properties, including size, shape and crystallinity, different from those of their inorganic counterparts, while some biominerals have geological equivalents that only form under the most severe conditions. For example, magnetite (Fe_3O_4) is a mineral that normally forms only under elevated temperatures and pressure in igneous and metamorphic rock, but several bacteria and vertebrates are able to produce it as a biomineral [9].

There are two different ways in which an organism exerts control over biomineralization. The first is referred to as "biologically-induced" [9,10] which refers to the process by which organisms induce mineralization as a by-product

of metabolic processes interacting with the surrounding environment. For example, some green algae precipitate calcium carbonates as a by-product of photosynthesis. The metabolic removal of carbon dioxide from saturated calcium bicarbonate solution produces calcium carbonate according to the chemical reaction,

$$Ca^{2+} + 2HCO_3^- \rightleftharpoons CaCO_3 + CO_2 + H_2O.$$

This method of indirect regulation often generates biominerals that have crystal habits much like those produced by precipitation from inorganic solutions [9].

Conversely, "biologically-controlled" mineralization, which is explored further in Section 1.3, involves much more control over mineralization. In this case, organisms, via genetic coding, direct the mineralization process with the help of specific biomolecules that nucleate and control the growth and morphology of the crystals [10].

The remainder of this thesis will focus on biomineralization in humans. A greater understanding of this process in the human body would be of significant medical relevance and is the motivation of this study. Such an understanding could lead to better bone repair therapies, implant development, and the prevention of serious unregulated biomineralization diseases such as vascular calcification and kidney stones as well as more benign conditions, like oral plaque calcification.

The primary role of biomineralization is to meet physiological needs for physical support and internal protection. In mammals, it is the process by which the skeleton and teeth are developed. Biomineralization is a dynamic process, and involves different mechanisms even within the same organism. For example, in vertebrates, mineralization occurs in calcified cartilage, bone,

cementum, dentin and enamel. One model for biomineralization involves the construction of an extracellular matrix, generally consisting of collagen and other proteins, followed by the acidic protein-controlled deposition of minerals in and around the collagenous matrix.

Hydroxyapatite

Hydroxyapatite, $Ca_{10}(PO_4)_6(OH)_2$ is the principal mineral component of bones and teeth, comprising on average 65% by weight of bone, cementum and dentin and 95% of enamel [4]. However bone mineral, or biological apatite, is not simply crystalline hydroxyapatite but is actually a "microcrystalline, non-stoichiometric, structurally imperfect analogue to hydroxyapatite" [11]. Bone mineral has a calcium deficiency of 5-10%, meaning that another ion has been substituted for the calcium ion. It also often contains carbonate ions (CO_3^{-2}) in place of the phosphate ions, and can readily incorporate a number of other ionic substitutions into its crystal structure. Almost half of the periodic table can be substituted into the apatite crystal structure in place of either Ca^{2+}, PO_4^{3-} or OH^- ions [11–13].

This compositional flexibility of biological apatite has physiological benefits. It allows the human skeleton to serve many functions, including acting as a source of calcium, phosphate, and carbonate to maintain cellular function, and removing heavy metal ions [13] from the blood stream. Calcium and phosphate ions serve many cellular functions and carbonate, which is available both on the bone surface as bicarbonate and inside the crystal, increases crystal solubility [12]. This compositional flexibility is the reason why dentists apply fluoride treatment to teeth, as substitutions of fluoride for hydroxide ions in the crystal lattice occurs readily and decreases apatite solubility.

Because of all the structural flexibility that biological apatite displays, a precise mineral formula for this material does not exist. As a matter of simplification, hydroxyapatite is commonly used as a model for biological mineralization and for orthopedic biomaterials [13]. We also refer to bone mineral as hydroxyapatite throughout this thesis.

Bone and Tooth Development

Bones and teeth are the major mineralized tissues within the body. Bones provide protection of internal organs, mechanical support and, in tandem with muscles, provide motility. Teeth are used to cut and chew food. Bone is a dynamic organ. It can be thought of as a "living mineral" as it constantly undergoes growth, dissolution and remodeling in response to internal signals and external forces [4]. For example, astronauts on the space station experience a loss of bone mass as a result of weightlessness [14]. Although the precise mechanism is not understood, bones exhibit piezoelectric effects [12], whereby the application of pressure produces electric charges which stimulate bone mineral growth. It is believed that the network of mineralized matrix-encased bone cells called osteocytes act as strain gauges. Mechanical stimulus of the bone is believed to trigger these osteocytes to emit electrochemical signals which in turn activate osteoblasts, or bone-building cells.

As indicated above, with the exception of enamel, bones and teeth are, on average, composed of 65% hydroxyapatite by weight, with the other 30% consisting of organic materials and approximately 5% water. In bone, 90% of the organic phase is collagen, with the remaining 10% consisting of various types of proteins [12]. The organic phase of bone serves two purposes. The first, which will be explored further in Section 1.3, is to provide the architec-

tural scaffolding for bone during its growth and development [4]. The second function is to give bone mechanical properties that naturally forming hydroxyapatite lacks. These include increased toughness and reduced stiffness, and depend on mineral content and the internal microstructure of the bone [4]. These properties can vary with the function of different bones. For example, a fast moving and agile creature requires more elastic bones with lower mineral content than a large marine animal. This is why the mineral content of deer bones is only 50%, while whale bones are roughly 80% mineral [4].

1.1.1 Pathological Mineralization

Pathological biomineralization can have undesirable effects. Some of the most severe examples include vascular calcification and kidney stones, the passage of which can be incredibly painful.

The Kidney Foundation of Canada claims that one in ten Canadians will develop kidney stones in their lifetime [15] and the prevalence of stone formation has been increasing in recent years [16]. Roughly 80% of kidney stones consist of calcium oxalate and calcium phosphate, while about 19% are composed of struvite ($(NH_4)MgPO_4{\cdot}6H_2O$) or uric acid ($C_5H_4N_4O_3$) [16].

Sufficiently small kidney stones can form and pass unnoticed. Once a stone becomes several millimeters in diameter however, it begins to cause renal colic, initially causing minor discomfort but culminating in extreme pain. [16].

Stones less than 5 mm in diameter have a high chance of being passed. For stones between 5 and 7 mm, there is approximately a 50% chance of passage, but stones larger than 7 mm require some form of medical intervention, including extracorporeal shock wave lithotripsy (ESWL), stone disruption using lasers, or surgical intervention. ESWL uses sound waves to disrupt the stone,

fracturing it into small pieces that can be passed without discomfort. Stone disruption with lasers involves inserting an endoscope up the ureter into the kidney pelvis to disrupt the stone with a high powered laser. Finally, surgical intervention involves a small incision in the flank of the patient and removal of the stone from the kidney [16].

Calcification of the vascular system is associated with aging, diabetes, and renal failure [17]. It is also a common consequence of biomaterial implants or prostheses such as prosthetic heart valves. Heart valve calcification leads to mechanical dysfunction and ultimately valve failure [17]. Vascular calcifications were once thought to occur passively from the precipitation of calcium phosphate salts, however it is now believed that there are two different mechanisms at work. Firstly, it appears that vascular calcification is a consequence of a regulated process including the deposition of an extracellular matrix, not unlike other physiological calcification processes [18]. The second mechanism is a loss of mineralization inhibitor proteins such as osteopontin, which results in an imbalance between the promotion and inhibition of calcification [18].

1.2 Crystal Nucleation and Growth

1.2.1 Nucleation

Crystallization of a mineral from solution is a phase transition that begins with a nucleation event, of which there are two types. As with most first order phase transitions, an energy barrier must be overcome before ions can precipitate out of solution to form a crystal. Heterogeneous nucleation occurs in the presence of a foreign substrate that reduces this energy barrier. The formation of biominerals is almost always initiated by heterogeneous nucleation. The

ability to facilitate the formation of stable nuclei depends on the nature of the substrate, and will be explored further in Section 1.3. The second possibility is homogeneous nucleation, which occurs spontaneously in the absence of any impurities. The difference between these two types of nucleation is illustrated by what occurs in freezing water. Normal tap water will freeze at around 0°C, because it contains numerous small suspended particles that act as nucleation points for ice formation. If the water is very pure and free of particulate matter however, it can be supercooled to temperatures well below zero. This is due to the fact that homogeneous nucleation must overcome a relatively large energy barrier (compared to that for homogeneous nucleation) before it can successfully initiate the phase transition. While homogeneous nucleation is the much less common phenomenon, it is worth exploring as the principles of the process are helpful in understanding heterogeneous nucleation [10].

Homogeneous nucleation occurs when solution is sufficiently supersaturated that ionic clusters of critical size form spontaneously. The formation of ionic clusters smaller than the critical size is energetically unfavourable, but if the ionic clusters reach the critical size, they will overcome this energy barrier and achieve a more stable, favourable state within the crystal lattice. This energy barrier is illustrated in Figure 1.1, which shows the free energy of nucleation as a function of the cluster radius r. The free energy has a maximum value at radius r^*. Figure 1.1 shows that a cluster smaller than the critical radius will dissolve back into solution. If it can spontaneously reach a size larger than the critical radius however, it will form a stable crystal nucleus and continue to grow [19]. The free energy of formation of a nucleus is given by

$$\Delta G_N = \Delta G_{surface} + \Delta G_{Bulk}, \tag{1.1}$$

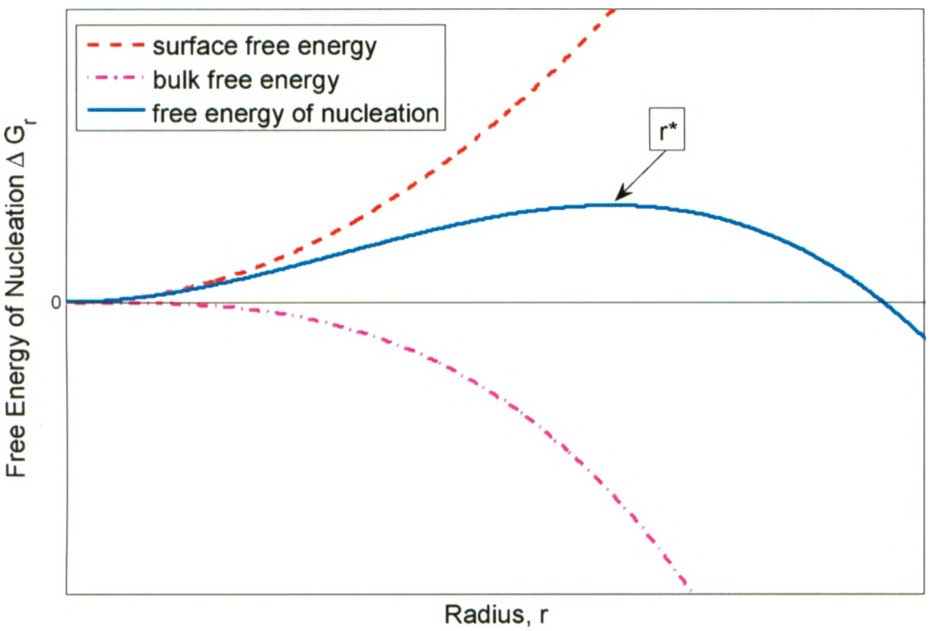

Figure 1.1: Gibbs Free Energy of Ionic Clusters

The total contribution to the Gibbs free energy of an ionic cluster as a function of radius. The red curve is the free energy due to surface tension. The purple curve is the free energy of the bulk crystal and the blue curve is the sum of these two contributions. At small r the surface free energy dominates and further growth of the cluster is unfavourable, so the cluster will redissolve. However, if r becomes larger than a critical size, r^*, the cluster will grow as a stable nucleus.

where ΔG_N is the free energy of formation for a given nucleus, $\Delta G_{surface}$ is the surface free energy due to the solid-liquid interface and ΔG_{bulk} is the free energy released by the formation of bonds in the crystal bulk. $\Delta G_{surface}$ and ΔG_{bulk} are defined by

$$\Delta G_{surface} = 4\pi r^2 \sigma \tag{1.2}$$

and

$$\Delta G_{bulk} = -\frac{4\pi r^3 \Delta G_v}{3V_m} \tag{1.3}$$

respectively, where r is the radius of the cluster, σ is the interfacial free energy per unit surface area, ΔG_v is the free energy change per mole associated with the phase change, and V_m is the molar volume. Inserting Equations (1.2) and (1.3) into Equation (1.1) yields

$$\Delta G_N = 4\pi r^2 \sigma - \frac{4\pi r^3 \Delta G_v}{3V_m}. \tag{1.4}$$

Equations (1.2), (1.3) and (1.4) are plotted in Figure 1.1. The free energy of nucleation has a maximum value, ΔG_N^* at a critical radius r^* that can be calculated by differentiating Equation (1.4) [10], corresponding to the activation energy required for the phase change to proceed. ΔG_N^* is given in terms of the degree of supersaturation of the solution by [10]

$$\Delta G_N^* = \frac{16\pi\sigma^3 v^2}{3(k_B T \ln S)^2}, \tag{1.5}$$

where S is the supersaturation, defined as c/c_o, where c is the ionic concentration in the solution and c_o is the ionic concentration when the system is saturated, v is the volume per molecule, k_B is the Boltzmann constant and T is the temperature.

ΔG_N^* can be regarded as an activation energy, and is related to the rate of nucleation J_N by

$$J_N = Ae^{-\Delta G_N{}^*/k_BT}, \tag{1.6}$$

where A is some constant.

From this discussion, it can be seen that the surface energy σ of the critical nucleus r^* and the degree of supersaturation S are the key determinants to crystal nucleation. Interestingly, both of these factors are subject to biological influence [10]. This will be explored further in Section 1.3.

1.2.2 Crystal Growth

Once a stable nucleus has formed, it is free to grow. Crystal growth is generally reversible, and the net growth rate is defined as the difference between the arrival and departure rates of atoms at the crystal surface. For a crystal to grow, more molecules need to bond to the surface than leave it, and this exchange occurs preferentially in certain places on the surface [10, 20]. A typical crystal surface has flat regions called terraces and steps which separate terraces at different levels. These steps often contain kinks, as illustrated in Figure 1.2. These kinks are important for the growth of the crystal because a molecule adhering to the kink increases the number of bonds it makes with the existing crystal. Conversely, when molecules leave the crystal to return to solution, they are more likely to leave from the kinks than from a complete step or within a terrace. As a result, the crystal growth rate scales with the kink density [19]. Once a step propagates to the end of the crystal face, however, it disappears and further growth becomes difficult as new layers are often slow to nucleate on a flat crystal surface [20]. Alternatively, defects in the crystal

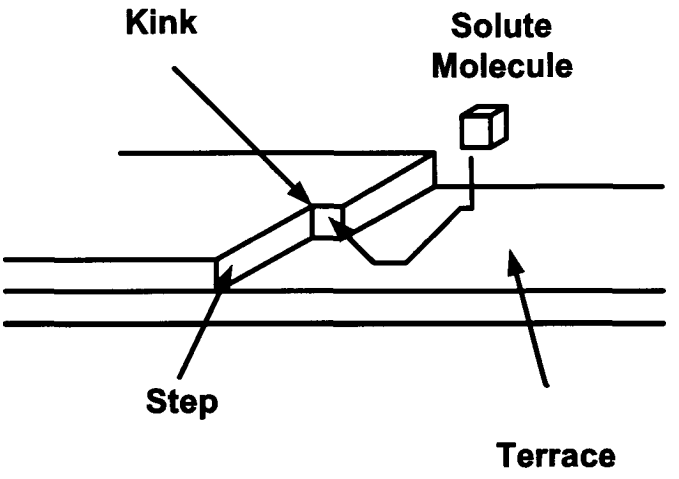

Figure 1.2: Kink and Step Diagram

A kink and step propagating across the face of a crystal. Molecules from the solution diffuse onto the crystal and dehydrate, or disrupt and displace the coordinated water molecules adsorbed to the crystal face. The molecules then diffuse across the crystal face until they encounter a kink and become incorporated into the crystal lattice, propagating the kink.

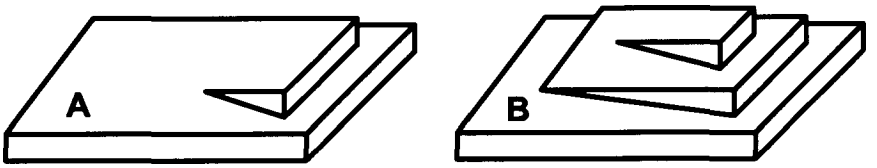

Figure 1.3: A Screw Dislocation Diagram

(A) demonstrates the early formation of a screw dislocation on a crystal face. (B) shows the screw dislocation some time later after it has propagated, generating several new layers on the crystal face. The propagation of screw dislocations creates new steps which facilitate continued crystal growth.

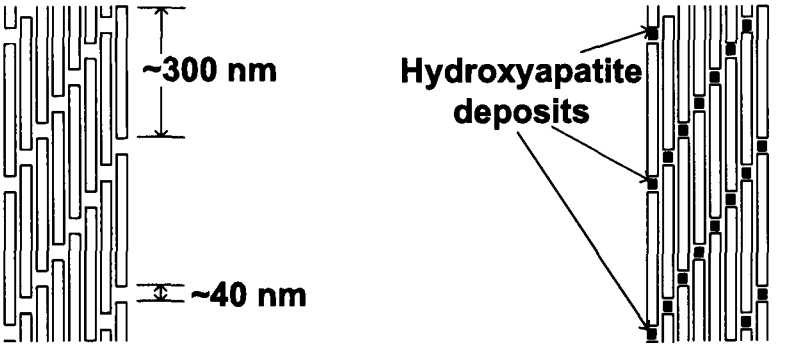

Figure 1.4: A Collagen Matrix Undergoing Mineralization

This schematic diagram illustrates the mineralization of a collagen matrix. In the precursor scaffold for bone known as the extracellular matrix, fibrilar collagen arranges itself in a staggered array, as this conformation maximizes chemical crosslinkings. The holes between successive collagen molecules act as nucleation sites for hydroxyapatite formation, a process which is believed to be initiated and regulated by noncollagenous proteins.

structure called screw dislocations can lead to the growth of new layers as shown in Figure 1.3. As the dislocation propagates it creates a screw-like structure on the crystal resulting in the creation of a series of new layers and more crystal growth than a typical kink.

1.3 Proteins in Biomineralization

Proteins are biological macromolecules consisting of well defined sequences of amino acids, called residues. After synthesis of a protein the constituent residues can be modified with what are called post-translational modifications which alter the properties of the protein. Proteins serve innumerable functions within the body.

The noncollagenous fraction of the organic component of bone consists of some 200 various proteins [4], with some more prevalent or relevant to the

mineralization process than others. As these proteins have been extracted and their bone-related roles investigated, a model has been developed that aims to explain the biologically-controlled mineralization process [4]. In short, collagen forms a structural framework, which is represented schematically in Figure 1.4. Certain proteins interact with the collagen and act to nucleate mineral within the gaps in the collagen, known as hole sites, while other proteins regulate the mineral growth process. Protein regulation of mineral growth will be addressed in Section 1.3.1. As the nucleated mineral grows, it expands beyond the collagen holes, eventually forming plates that surround the collagen.

This model is motivated by empirical evidence based on the proteins that have been extracted from the extracellular matrix. Collagen itself has been shown not to nucleate hydroxyapatite formation [4], but is believed simply to be the structural framework within which mineralization occurs. Conversely, some of the noncollagenous proteins that have been extracted from bone have been demonstrated to bind to hydroxyapatite crystals and to affect their growth and development *in vitro*. In particular, acidic proteins containing attached phosphate groups, called phosphoproteins, are believed to be responsible for initiating and controlling the growth of hydroxyapatite [21–30].

In this thesis, we focus principally on the effects of osteopontin (OPN) on hydroxyapatite formation, though other proteins have similar effects on mineralization [24, 25, 29]. Bone sialoprotein (BSP) and OPN are both phosphosialoproteins enriched with acidic amino acid residues, and have similar physical properties [22]. However they have been demonstrated to exhibit completely different effects on hydroxyapatite formation [22, 24].

Bone sialoprotein is a protein of approximately 320 residues. It is highly negatively charged, has a flexible structure, and is rich in glutamic acid residues, which are distributed along its length as well as in two clusters of up to ten con-

secutive residues [31]. BSP is essentially only found in mineralized tissues and is generally expressed at sites of *de novo* bone formation [23]. It readily binds to collagen in the extracellular matrix [28]. Most importantly, however, BSP has been shown to directly nucleate hydroxyapatite at concentrations well below the threshold for spontaneous precipitation of calcium phosphate [22–24]. It has also been suggested that the active sites of nucleation on the protein comprise the two contiguous glutamic acid clusters with contributions from specific phosphorylated serine residues [23].

Although OPN has a similar structure to BSP, it does not nucleate hydroxyapatite, but rather is a potent inhibitor of its formation and growth [24, 29]. OPN is approximately 300 residues in length [32]. It is a disordered protein, which means that it is flexible and lacks secondary structures like alpha-helices [33]. It is also highly negatively charged, containing a large number of aspartic and glutamic acid residues and one contiguous aspartic acid sequence. Rat bone OPN has approximately 30 potential phosphorylation sites [34, 35], though on average only 10 phosphates are found per molecule. Milk OPN (bovine and human) contains 30 or more phosphate groups [36]. OPN is one of the most abundant noncollagenous proteins found in bone [37], but it is also found in all bodily fluids [38]. It is expressed by cells in bone, kidney, uterus, lungs, and the gastrointestinal tract [39]. OPN is involved in a number of physiological processes besides biomineralization, including cancer metastasis, immunity, apoptosis, inflammation, and wound healing [37, 40].

Osteopontin is widely regarded as a good inhibitor of hydroxyapatite [41] and calcium oxalate [42, 43] crystallization, but the primary mechanism behind this inhibition is still a subject of debate. The aspartic and glutamic acid residues of OPN and BSP are believed to be responsible for allowing them to bind tightly to hydroxyapatite [7]. Constant composition experiments, how-

ever, on aspartic and glutamic acid peptides alone demonstrate that aspartic acid is 1000 times more potent at inhibiting hydroxyapatite growth [44]. It has been suggested that OPN inhibits hydroxyapatite growth via its contiguous aspartic acid region [22,45]. It has also been demonstrated that phosphorylations play an important role in OPN's inhibitory activity, with non-phosphorylated OPN being a much less potent inhibitor [44, 46].

It has also been suggested that the order of the residues of OPN is significant [47]. Pampena *et al.* studied a series of synthetic phosphorylated OPN-derived peptides using the constant composition method. They found that increasing the concentration of the peptides caused an increase in the lag time before precipitation occurred, but did not actually prevent the formation of crystals. They then created a new peptide which contained all of the amino acids of one of the OPN-derived peptides, but rearranged in a random sequence. The inhibitory potency of this "scrambled" peptide was reduced by almost one half [47].

Two groups have performed molecular dynamics simulations in an effort to better elucidate the inhibition mechanism, and have come to slightly different conclusions [42, 48]. Wang *et al.* simulated phosphorylated 14-mer peptides of OPN in the presence of calcium oxalate and came to the conclusion that local binding of phosphate structures is responsible for the inhibition of crystal growth [42]. On the other hand, Grohe *et al.* used molecular dynamics to study three forms of the same peptide, differing only in phosphate content, interacting with a calcium oxalate monohydrate crystal surface [48]. The three peptides had the same primary amino acid sequence, but different numbers of phosphorylations. These simulations demonstrated that phosphate groups were important for drawing the peptide close to the crystal face, but did not actually make contact with the crystal surface. Grohe *et al.* suggest that

carboxylate groups on the aspartic and glutamic residues are responsible for binding the protein to the crystal face [48].

The average person excretes about 6 mg of OPN per day in their urine [49], regardless of urine volume [50]. Human urine is also supersaturated with respect to calcium oxalate, but people do not generally form kidney stones [43]. This has led to the suggestion that OPN plays a role in preventing the formation of kidney stones. This suggestion is reinforced by the fact that OPN is generally found in kidney stones in average concentrations of 8 mg/g of stone [50].

Wada *et al.* have demonstrated that soluble OPN is an inhibitor of vascular calcification, and increased synthesis of OPN that has been observed near sites of vascular calcification could indicate a physiological attempt to limit or prevent the calcification from occurring [30].

Finally, the absence of OPN in genetically modified mice has been shown to have a direct effect on the way bones are formed. Boskey *et al.* studied the bone in OPN-knockout mice and showed that with aging, there was an increased mineral density in their bones compared to control mice. The same mice possessed increased crystallinity throughout their skeleton compared to the controls [51].

1.3.1 Biomineral Growth Modification

Proteins can affect the growth and formation of biominerals in several ways. Nucleator proteins like bone sialoprotein can act as sites of heterogeneous nucleation, acting to dramatically reduce the activation energy [41] and increase the rate of nucleation. It is conceivable that certain proteins could reduce the activation energy of nucleation selectively to favour one polymorph over

another, resulting in a preferred mineral structure [4].

Alternatively, proteins that bind sufficiently tightly to crystal faces can inhibit crystal growth by a process known as step blocking, whereby the protein acts to block attachment of molecules at a step edge. Kink blocking can also occur when the protein molecule binds to a kink site, decreasing the kink site density and slowing the kink propagation. [19]

Finally, a protein molecule could inhibit growth simply by preventing nucleation from occurring. If a long and flexible molecule enveloped a nucleating ion cluster before it achieved its critical size, preventing it from growing further, the sub-critical nucleus would redissolve [41].

1.4 Current Methods of Assessing the Role of Bone-Related Proteins

The goal of this work was to develop a technique that could be used to measure inhibitory potency and kinetic parameters such as growth rates and particle sizes that cannot be readily determined using current techniques. Currently a number of different approaches are used to explore the relationship between bone-related proteins and hydroxyapatite nucleation and growth. These include the constant composition and the steady state methods, which will be described briefly in this section.

The Constant Composition Method

The constant composition method is illustrated in Figure 1.5. It is a versatile technique that can be used to assess the potency of crystal nucleation and inhibition proteins, by measuring *de novo* crystal formation or growth of seed

crystals. Here the method of studying seeded crystal growth in the presence of inhibitor proteins will be described. The constant composition method uses a feedback loop to ensure that the composition of a calcium phosphate solution remains constant throughout the course of the experiment, in an effort to reflect *in vivo* conditions.

Seed hydroxyapatite crystals are added to a continually mixed solution of metastable calcium and phosphate ions at pH 7.40. As the hydroxyapatite crystals begin to increase in size, they incorporate OH^- ions into their structure, which depresses the pH. This drop in pH triggers a computer-controlled titrator which injects a fresh supply of calcium, phosphate and sodium hydroxide ions into the solutions until the pH returns to 7.40. Nitrogen gas is also bubbled through the solution to prevent the dissolution of carbon dioxide, which would artificially depress the pH. When inhibitor proteins are added to the calcium phosphate solution, the rate of growth of the crystals decreases, so less titrant is required over the course of the experiment. The crystal growth rate can be calculated from the amount of titrant required to maintain a constant pH over the course of the experiment. Comparing the growth rate in the presence of the inhibitor to the results of control experiments gives a measure of the protein's inhibition potency. A related system known as auto-titration functions similarly, but does not replenish the supply of calcium and phosphate ions. These systems have been successfully used to assess the inhibitory potency of BSP, OPN and a number of other bone-related proteins [24,44,47,52]. The primary drawbacks of this technique are that it is technically challenging to maintain appropriate conditions and is time consuming.

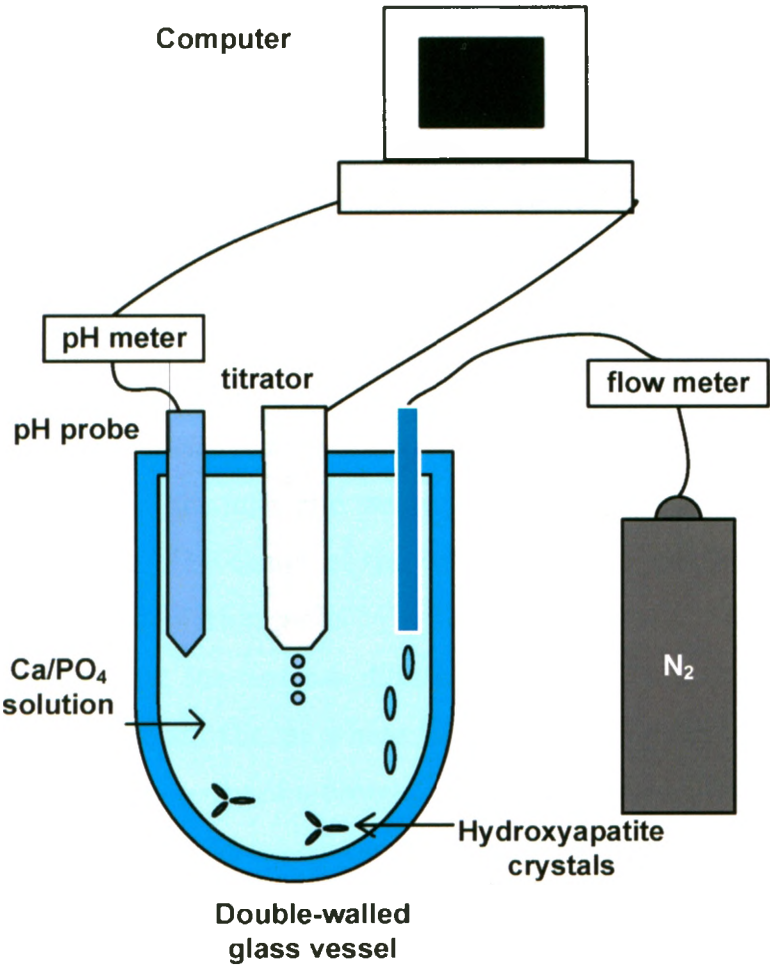

Figure 1.5: The Constant Composition Method

This method is commonly used to assess the inhibitory potency of bone-related proteins. See text for details.

The Steady State Method

The steady state method is generally used to assess the potency of crystal nucleator proteins. This method, illustrated in Figure 1.6, involves a number of plastic cells arranged in series. In Figure 1.6, calcium solution is continuously pumped, via the top left inlet into the cell. The bottom left outlet of the cell leads to a reservoir where the waste calcium solution is collected after it has passed through the cell. Similarly, phosphate solution is pumped into the cell via the top right inlet and waste phosphate is removed through the bottom right outlet. The center of the cell contains an agarose gel which is separated from both solution paths by a dialysis membrane. As the solutions pass through the cells, the ions can diffuse across the membrane into the gel, and then diffuse through the gel where they establish a concentration gradient. The nucleation potency of a protein can be assessed by incorporating the protein into the gels at different concentrations and determining the concentrations at which nucleation of hydroxyapatite occurs. Control experiments are performed in the absence of protein. After the experiment has run its course, the gels are removed and calcium and phosphate content is determined. This method has been used to assess the nucleation potency of BSP, BSP-derived peptides and other bone-related proteins [22–24, 29]. The primary drawback of this method is that it is time consuming, with one experiment taking at least five days to run. Furthermore, it reveals nothing about the mechanics or kinetics of the nucleation process, but only whether or not mineralization occurred.

1.5 Purpose of Thesis

Conventional methods of studying the effects of proteins on crystal growth are time consuming. The development of a fast, convenient and reliable method for assessing the potency of inhibitor or nucleator proteins would be a welcome and useful development in the field of biomineralization research.

The goal of this study was to investigate the use of dynamic light scattering for this purpose and to validate the technique by studying several known inhibitor proteins and peptides.

This study demonstrates that dynamic light scattering does provide a fast and reliable method for assessing the roles of proteins in the biomineralization process and readily provides information not easily obtainable through other means.

Chapter 2

Light Scattering

2.1 Introduction

Dynamic light scattering, which is the technique used in this work, is often used to measure the size and size distribution of small particles [53]. For example, it has been used to study the nucleation and growth kinetics of zeolitic (aluminosilicate) particles [54–56] and gibbsite (γ-$Al(OH)_3$) [57] from solution, to assess protein-protein interactions, and to measure crystallization kinetics [58–60] and protein folding kinetics [61]. Onuma *et al.* have used light scattering to measure the molecular growth units of hydroxyapatite crystals [62, 63], and to monitor the crystallization of hydroxyapatite around so-called growth factor proteins. Their interest was in constructing a protein-crystal (fibroblast growth factor - HA) composite that could be used to better induce bone repair [64]. In this thesis we investigate the use of dynamic light scattering to study the effects of a bone-related protein and synthetic peptides on the nucleation and growth of hydroxyapatite crystals.

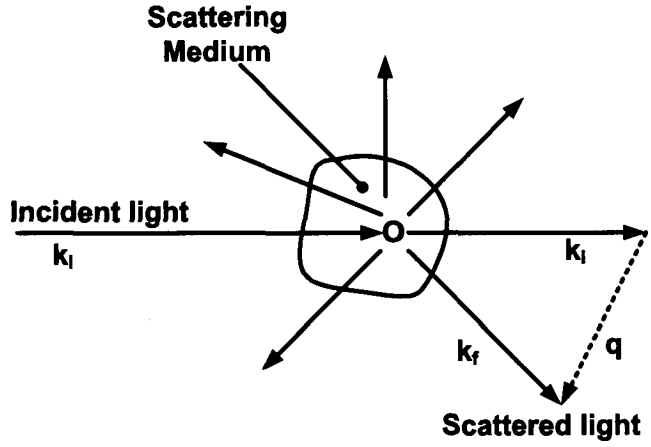

Figure 2.1: A Schematic Illustration of Light Scattering

The incident light enters the medium from the left. While most of the light passes through the volume unaffected, some is scattered and measured by a detector. $\mathbf{q}$ is the scattering vector, which is defined as the difference between the propagation vectors of the scattered and incident beams, $\mathbf{k}_f$ and $\mathbf{k}_i$ respectively.

2.2 Light Scattering

The light scattering process is represented schematically in Figure 2.1. In this figure, radiation with wave vector $\mathbf{k}_i$ is incident on a scattering medium from the left [65]. In our experiments, the scattering medium is a suspension of small calcium phosphate precipitates, some to most of which are hydroxyapatite crystals. Most of the radiation passes through the medium unaffected, but some will be scattered by the suspended particles. A detector positioned at an angle θ relative to the incident radiation measures the intensity of the scattered radiation, $I(\theta, t)$. The scattering particles diffuse through the medium over time, so $I(\theta, t)$ fluctuates. The scattering volume V is defined as the region that is both illuminated by the incident beam and observed by the detector [65,66].

The scattering vector $\mathbf{q}$ is defined by $\mathbf{q} = \mathbf{k}_f - \mathbf{k}_i$, as shown in Figure

2.1, where $\mathbf{k}_f$ and $\mathbf{k}_i$ are the propagation vectors of the scattered and incident beam respectively. If q is the magnitude of the scattering vector $\mathbf{q}$, it follows that

$$q^2 = |\mathbf{k_f} - \mathbf{k_i}|^2 = k_f^2 + k_i^2 - 2\mathbf{k_i} \cdot \mathbf{k_f}. \tag{2.1}$$

In this work we assume that the light is scattered quasielastically, so $|k_f| \approx |k_i|$. Using the law of cosines, $k_i \cdot k_f = k_i k_f \cos\theta = k_i^2 \cos\theta$, so Equation (2.1) becomes

$$q^2 = 2k_i^2 - 2k_i^2 \cos\theta = 2k_i^2(1 - \cos\theta) = 4k_i^2 \sin^2(\theta/2). \tag{2.2}$$

Since $k_i = 2\pi/\lambda$, where λ is the wavelength of the light in the scattering medium, q is given by

$$q = \frac{4\pi n_o}{\lambda_\circ} \sin\left(\frac{\theta}{2}\right), \tag{2.3}$$

where n_o is the refractive index of the scattering medium and $\lambda_\circ$ is the wavelength of the light in vacuum.

In static light scattering measurements, the time averaged scattered intensity is measured as a function of scattering angle, or equivalently as a function of q. Static light scattering measurements provide structural information about the scatterers [67, 68]. For example, static light scattering can provide information about the molecular weight, radius of gyration and sometimes the shape of scatterers [69].

2.3 Dynamic Light Scattering

In dynamic light scattering, the fluctuations of the scattered intensity are measured and analyzed as a function of time. Dynamic light scattering provides

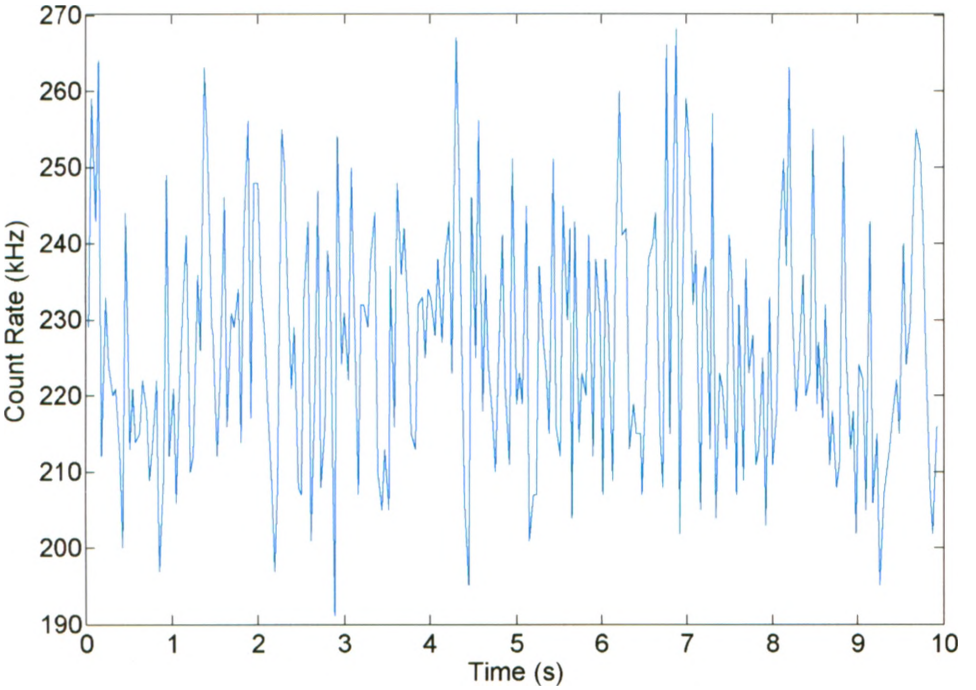

Figure 2.2: A Typical Scattered Intensity Plot

A typical plot of $I(t)$, showing the fluctuations of the scattered intensity as a function of time. These data were obtained from a measurement using a suspension of 220 nm polystyrene spheres at a scattering angle of 90°.

information about the diffusion and hydrodynamic radius of the scatterers in the medium.

A suspension of colloidal particles illuminated by coherent light will produce a grainy speckle pattern when viewed in the far field [53]. At some points, the light scattered by the particles interferes constructively, and at others, destructively, resulting in regions of high and low intensity. The scatterers undergo Brownian motion, causing the interference pattern to change with time and generating random fluctuations in the speckle pattern. A typical plot of the randomly fluctuating scattered photon intensity as a function of

time is shown in Figure 2.2. The scattered intensity and the photon count rate are used interchangeably throughout this thesis because intensity is proportional to the number of photons incident on the detector in time, given that the photon energy and the detector size are fixed. The intensity fluctuations are analysed by calculating the time autocorrelation function of the scattered intensity at the detector, $g^2(\tau)$, defined by

$$g^2(\tau) = \frac{\langle I(t)I(t+\tau)\rangle}{\langle I(t)\rangle^2}. \tag{2.4}$$

The intensity autocorrelation compares the intensity $I(t)$ at some time t to its value $I(t+\tau)$ a time τ later. The angle brackets indicate an average over all times t. When $\tau = 0$, the two signals are the same, and $g^2(\tau)$ is a maximum. As τ increases, $I(t)$ and $I(t+\tau)$ become less correlated and $\langle I(t)I(t+\tau)\rangle$ decreases. The radius of the scatterers, which is the quantity of interest in the present work, is actually calculated from the time autocorrelation function of the electric field. We measure the intensity because the electric field cannot be measured directly [53]. The electric field correlation function, $g^1(\tau)$, is related to the intensity correlation function, $g^2(\tau)$, by the Siegert equation [53],

$$g^2(\tau) = 1 + \beta \left[g^1(\tau)\right]^2, \tag{2.5}$$

where β is a constant related to the area of the detector.

For a monodispersed system, the electric field autocorrelation function decays exponentially with the delay time τ,

$$g^1(\tau) = e^{-Dq^2\tau}, \tag{2.6}$$

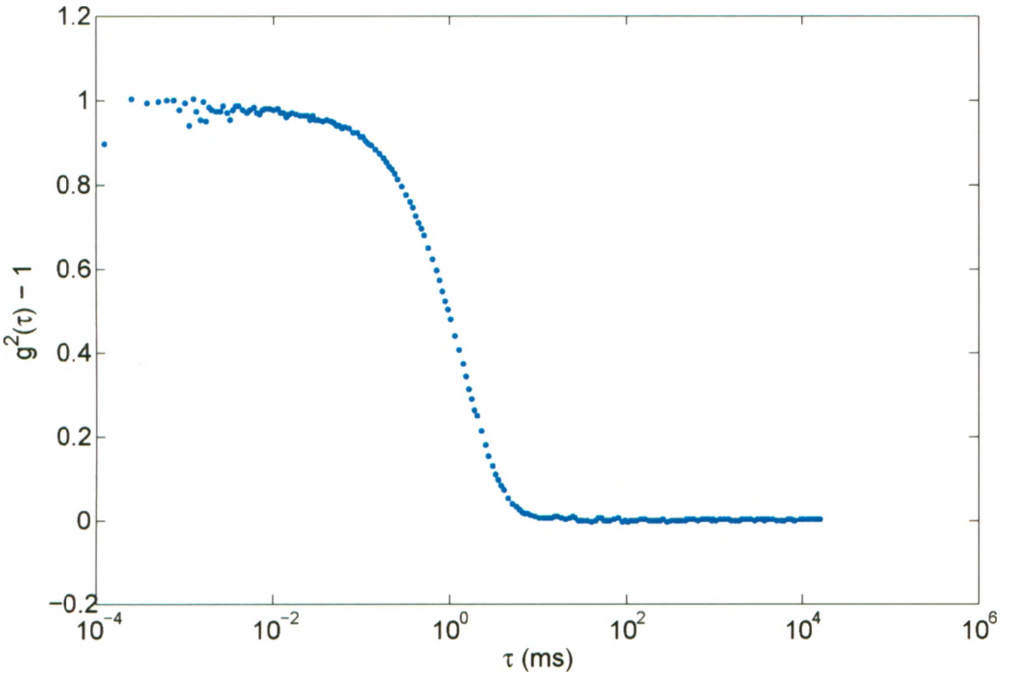

Figure 2.3: A Typical Plot of $g^2(\tau) - 1$

A plot of a typical intensity autocorrelation function. These data were obtained from measurements at a scattering angle of 90° on a Ca^{2+} PO_4^{3-} solution that had aged for 110 minutes producing a hydroxyapatite crystal suspension.

where D is the diffusion coefficient, given by Equation (2.7),

$$D = \frac{k_B T}{6\pi\eta r}. \tag{2.7}$$

Here k_B is the Boltzmann constant, T is the temperature, η is the viscosity of the solvent and r is the hydrodynamic radius of the particles. Equation (2.6) can be generalized for a polydisperse system to a sum of two or more exponential decays [70].

The light scattering device used in this work was a CGS-3 compact goniometer system manufactured by ALV. It is pictured schematically in Figure 2.4. It consists of four main parts: a laser, a goniometer, a detector, and a correlator. The laser source is a continuous wave HeNe laser of wavelength 632.8 nm and maximum power 22 mW.

The goniometer determines the scattering geometry and houses the sample in an index matching vat. The sample to be studied is placed in a 10 mm diameter, optical quality, cylindrical glass cuvette, which is in turn placed into a holder in the index matching vat. The vat is filled with toluene, which has a refractive index matching that of the cuvette. This is necessary to minimize scattering and refraction from the cuvette itself. The scattered light reaches the detector by passing through a narrow window located around the circumference of the vat.

The photomultiplier detector is positioned on the detector arm of the goniometer, which rotates about the center of the vat to give scattering angles θ between 12° and 155°. The experiments described in this thesis were all performed at $\theta = 90°$, corresponding to a scattering vector of 17 μm^{-1}. The distance of the detector from the scattering volume is set such that only one

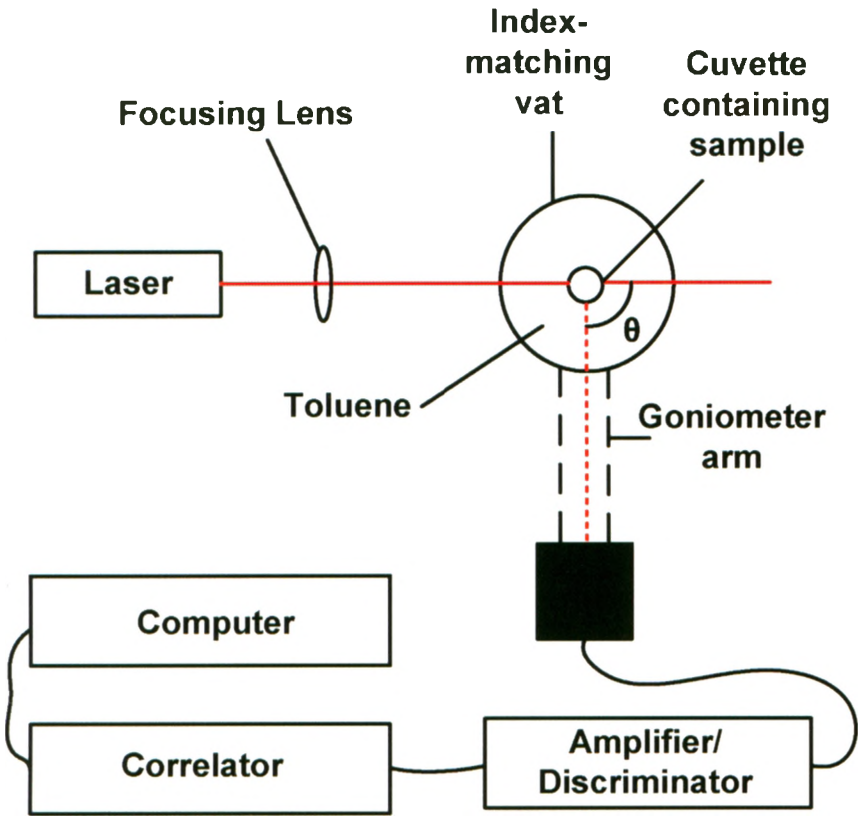

Figure 2.4: DLS Schematic

A schematic for the Dynamic Light Scattering device used in this experiment. Laser light is focused into the cuvette containing the sample. Light is scattered in all directions by the medium. Some of the light is measured at a scattering angle θ determined by the position of the detector. The intensity fluctuations measured by the detector are passed through the amplifier/discriminator where the pulses are digitized, and relayed to the correlator. The correlator generates the normalized intensity time autocorrelation function in real time and passes this to the computer.

or two speckles are measured.

The output signal from the photomultiplier detector is passed to a pulse amplifier/discriminator circuit that applies a threshold filter to remove spurious pulses and converts the signal to standard logic pulses of well defined height and duration [71]. The filtered, digitized signal is then passed to the correlator, which calculates the intensity autocorrelation function in real time. The intensity autocorrelation function is then sent to a personal computer along with the intensity-time data. A computer program performs curve fitting to calculate the distribution of hydrodynamic radii of the scatterers and displays the results.

Chapter 3

Materials and Methods

3.1 Calcium Phosphate Solution Preparation

It took a considerable amount of time and effort to determine a preparation method and solution concentrations that produced reliable and reproducible behaviour. It was noted that if the solutions were permitted to age more than 24 hours, their behaviour would change — sometimes they would become more reactive, sometimes less. Similar issues have been observed with both the steady state and constant composition methods (P. Azzopardi, private correspondence). For this reason, the solutions were prepared fresh daily from concentrated stock solutions. In particular, the Ca^{2+} solution was difficult to work with. It was determined that addition of NaCl or a buffering agent to the calcium-containing solution limited the stability of the prepared mixture.

Concentrated stock solutions of 1 M calcium chloride ($CaCl_2$), 0.5 M sodium phosphate dibasic (Na_2HPO_4), 2 M sodium chloride (NaCl), 1 M Tris (hydromethyl amino methane) ($C_4H_{11}NO_3$), and 0.5 M sodium azide (NaN_3) were prepared. All chemicals were obtained from Sigma Aldrich (St. Louis MO),

and stocks were prepared in MilliQ quality water. The stocks were filtered using 0.2 μm filters (Nalgene) and stored in clean, autoclaved glass bottles. From these stock solutions, three solutions were prepared daily: 12 mM Ca^{2+}, a 18.75 mM PO_4^{3-} and 18.75 mM Tris buffer. The PO_4^{3-} solution also contained 300 mM NaCl and 18.75 mM Tris buffer, while the 18.75 mM Tris buffer solution also contained 150 mM NaCl. All three solutions contained 0.02 % sodium azide by weight to prevent bacterial contamination. The PO_4^{3-} and Tris buffer solutions were then both adjusted to a pH of 7.40 by the addition of HCl (Sigma Aldrich). The addition of NaCl and the pH of 7.40 were to mimic *in vivo* conditions. After these solutions were prepared, approximately 50 ml of each was filtered through 0.2 μm or 0.02 μm syringe filters into sterile BD Falcon tubes. The 0.2 μm filters were insufficient to remove the contaminants from the Ca^{2+} solution, so it was filtered with 0.02 μm syringe filters obtained from Whatman (Maidstone, England). We found that these solutions, prepared daily, gave consistent and reproducible behaviour.

3.2 Protein and Peptide Preparation

We studied the effect on calcium phosphate and crystal growth of two proteins and two peptides. The proteins investigated were native rat bone osteopontin (nOPN) and recombinant rat bone osteopontin (rOPN). Recombinant OPN has the same amino acid composition as nOPN but lacks the post translational modifications, including the phosphates that are found in nOPN. In addition, two OPN-related peptides previously shown to modulate mineral formation in vitro [72], were studied: phosphorylated osteopontin poly-aspartic acid region (pOPAR), a synthetic 16mer peptide based on the OPN 65-80 sequence which includes a phosphorylated-serine residue and the contiguous aspartic

acid sequence; and a synthetic poly(aspartic acid) (Sigma Aldrich), with a mass of 11 kDa and containing approximately 95 residues. Both the nOPN, which was extracted and purified [73], and the rOPN, which was expressed in prokaryotic cells and purified [74], were prepared by H. Chen. The pOPAR was synthesized and purified by Y. Liao.

The proteins used in this study were provided in pre-weighed, freeze-dried aliquots. A protein aliquot was dissolved into a volume of the filtered Tris buffer solution, then a small volume was removed and further diluted with buffer. Several different concentrations of proteins/peptides were prepared, as described in Table 4.3. The diluted protein and peptide solutions were kept frozen at -20° C until required for the experiment.

3.3 Polystyrene Spheres

Light scattering measurements were also performed on suspensions of polystyrene latex spheres, to determine a relationship between particle size, particle number concentration, and scattered intensity. Spheres with refractive index of 1.59, density 1.05 g/cm^3 and radii of 15, 45 and 110 nm were purchased from Thermo Fisher Scientific (Fremont CA).

Chapter 4

Results

4.1 Polystyrene Spheres

We performed static light scattering measurements on several sizes and concentrations of polystyrene spheres in order to establish an approximate relationship between the size and number of scattering particles and the scattered intensity measured by the detector. A known mass fraction of spheres was suspended in water. The number density of spheres in this suspension is given by n_o, which is given by

$$n_o = \frac{1}{v_s\left(1 + \frac{\rho_s}{\rho_w}\frac{1-C}{C}\right)}, \tag{4.1}$$

where v_s is the volume of one sphere, ρ_s is the density of the spheres, ρ_w is the density of water, and C is the mass fraction of the spheres.

The experiments were each performed at a scattering angle of 90° for three consecutive one minute measurements. The average time-averaged scattered intensity for these three measurements is then plotted against the concentra-

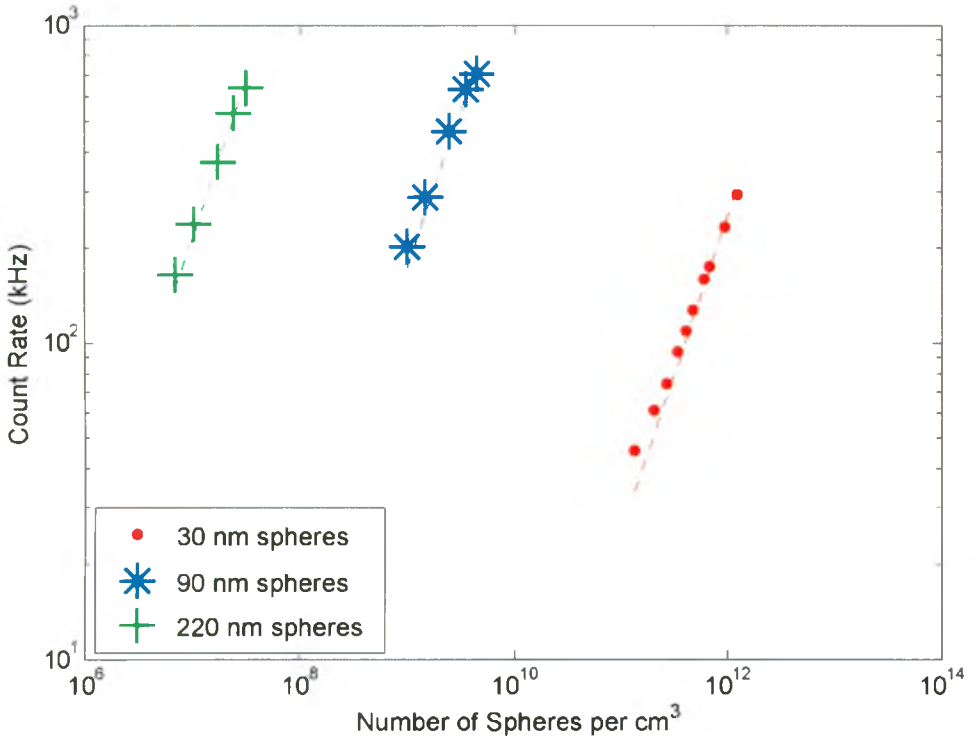

Figure 4.1: Count Rate vs Particle Concentration

The average count rate vs. the number of particles per cm^3 for spheres of radii 15, 45 and 110 nm at an angle of 90°. The lines are fits to the functions $2.52 \times 10^{-10} n_\circ$, $1.70 \times 10^{-7} n_\circ$, and $2.14 \times 10^{-5} n_\circ$ corresponding to the 15, 45, and 110 nm radii respectively.

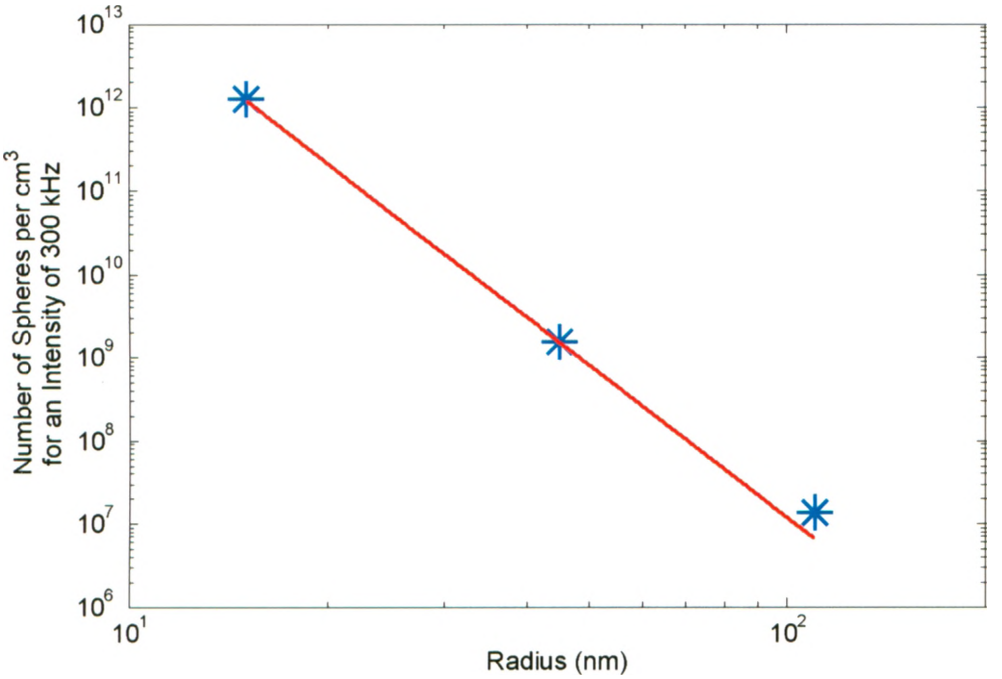

Figure 4.2: Number of Particles per cm^3 vs Radius for a Common Scattering Intensity

The number of particles per cm^3 vs. their respective radii for a scattering intensity of 300kHz.

Table 4.1: Fit Functions to Sphere Data

Sphere Radius (nm)	Slope (kHz cm^3/number)
15	$(2.5 \pm 0.1) \times 10^{-10}$
45	$(1.7 \pm 0.2) \times 10^{-7}$
220	$(2.1 \pm 0.1) \times 10^{-5}$

The parameters of the three functions fit to the data in Figure 4.1.

tion of the suspension in Figure 4.1. These data were fit to straight lines, the slopes of which are listed in Table 4.1. These fit functions describe the data well in all cases, indicating that the scattered intensity increases linearly with the number density of scatterers.

The same data were used to determine the relationship between the scattered intensity and the size of suspended scatterers. For each particle size, the concentration required to give a scattering intensity of 300 kHz was determined from the previous fits. The results are plotted in Figure 4.2. A power law fit to the data gives $I = (1.8 \pm 0.2) \times 10^{19} r^{(-6.09 \pm 0.05)}$ with I in kHz and r in nm, where r is the radius of the spheres. This fit describes the data well. Furthermore, this result is consistent with the theoretical treatment in ref. [69], where it is shown that the scattered electric field E from a small scatterer is proportional to the polarizability α, of the scatterer, which is in turn proportional to r^3. Since $I = E^2$, this implies that $I \propto r^6$.

Finally, we performed dynamic light scattering measurements on suspensions of the spheres using observation times and concentrations similar to those used in our crystallization experiments to confirm the accuracy of the radius measurements obtained from the light scattering system and its data analysis software. Table 4.2 shows the results, which consistently gave radii for the spheres equal to the expected values, within the uncertainty specified by the

Table 4.2: Sphere Size and Measurement Data

Sphere Radius(nm)	Measured Radius (nm)
15 ± 5	17.9 ± 0.2
45 ± 7	45.7 ± 0.2
110 ± 1	111 ± 1

The radii of the polystyrene spheres given by the manufacturer, along with the sizes measured by dynamic light scattering.

manufacturer of the spheres.

4.2 Protein-Crystal Measurements

Experimental Details and Behaviour

In our experiments, we studied the precipitation of small calcium phosphate crystals from the three solutions described in Chapter 3 by mixing 0.38 ml of the Ca^{2+} solution with 0.38 ml of the PO_4^{3-} solution in the presence of 1.04 ml of the Tris buffer solution. The concentrations in the final 1.80 ml solution were 2.53 mM Ca^{2+}, 3.96 mM PO_4^{3-}, 14.8 mM tris buffer and 150 mM NaCl. For the experiments involving the protein or peptide, 20 or 40 μl of dissolved peptide or protein solution was added to the mix, and an equal volume of Tris buffer solution was withheld. This ensured that the final mixed volume and concentrations were the same, and that the solutions differed from the controls only by the presence of the protein or peptide.

We performed control measurements using the above solutions prepared without any protein or peptide. All control experiments showed very similar behaviour. In general, for the first few minutes of observation, the scattered intensity would remain near the background level. The background scattering

intensity was determined to be 7 ± 1 kHz by averaging the scattered intensity using the Tris buffer solution for five minutes. Figure 4.3 shows the scattered intensity five minutes into a control measurement. The scattered intensity increases fairly rapidly, as in this figure, for about 30 minutes as the precipitate forms in the solution, then continues to increase more slowly for the remainder of the measurement. Figure 4.4 shows the scattered intensity 110 minutes into a control measurement, at which time the average intensity is slowly increasing. The average scattered intensity at the end of a control measurement, at 120 minutes, was approximately 85 kHz.

Each solution was observed for a period of two hours. Over this period, a new 60 second measurement was made every minute, and every five minutes the software would average the scattered intensity and hydrodynamic radii from the previous five minutes and save the results. This allowed for the collection of 24 data points over the lifetime of each solution. The samples were all tested in triplicate, and controls were run intermittently between the protein and peptide measurements to monitor for solution deterioration. Thus, the first, third and fifth measurements were control measurements and the second, fourth and sixth measurements were solutions with a peptide or protein. This allowed us to monitor any drift that may have occurred over the 12 hour measurement period. The concentrations of the proteins and peptides that we studied are given in Table 4.3.

Average Scattered Intensity

The five minute average scattered intensity values, $\bar{I}(t)$, for a typical control experiment and for the three concentrations of nOPN that we studied are plotted as a function of time in Figure 4.5. The control measurement had

Table 4.3: Protein and Peptide Concentrations Studied

[nOPN] μg/ml	[rOPN] μg/ml	[pOPAR] μg/ml	[poly-asp] μg/ml
0.052	1.13	1.39	0.083
0.103	4.55	11.1	0.33
0.414	9.10	44.4	0.67

The three concentrations tested for each protein or peptide.

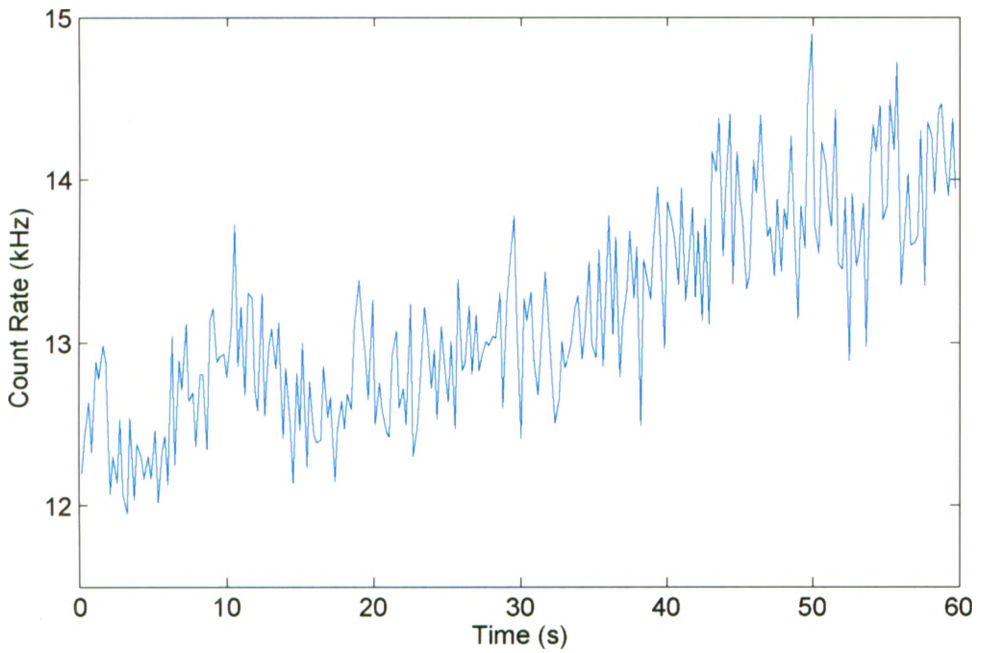

Figure 4.3: Early Count Rate vs. Time

The count rate as a function of time early in a typical control measurement. Here the 0 on the time axis corresponds to 5 minutes after the start of the experiment.

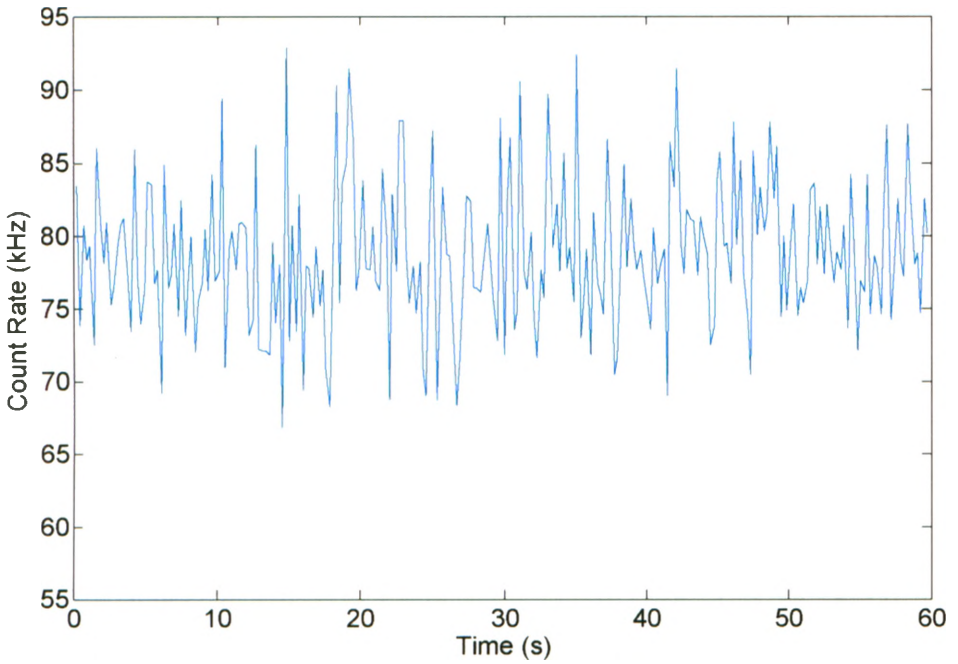

Figure 4.4: Late Count Rate vs. Time

The count rate as a function of time late in a typical control measurement. Here the 0 on the time axis corresponds to 110 minutes after the start of the experiment.

the highest $\bar{I}(t)$ by the end of the measurement, with the intensity decreasing with increasing protein concentration. The lowest concentration of nOPN, 0.052 μg/ml, decreased the final scattered intensity by about 15% while a concentration of 0.103 μg/ml reduced the final scattered intensity by approximately 50% below the control level. The highest concentration, 0.414 μg/ml of nOPN gave a constant scattering intensity at the background level.

Figure 4.6 is a plot of $\bar{I}(t)$ as a function time for a typical control and the three concentrations of poly(aspartic acid) that we studied. Once again, the control measurement gave the highest $I(t)$ with the intensity decreasing with an increase in protein concentration. The 0.083 μg/ml poly-asp solution only marginally reduced the final scattering intensity below the control measurement, while the 0.33 and 0.67 μg/ml solutions of poly-asp both gave low but slowly increasing and statistically similar intensities just above background level.

Analysis of the effect of pOPAR on calcium phosphate precipitation is depicted in Figure 4.7. $\bar{I}(t)$ values are plotted against time for a control and three different concentrations of pOPAR. The lowest concentration of pOPAR, 1.39 μg/ml, had a similar scattered intensity profile to that of the control. At 11.1 μg/ml pOPAR, $\bar{I}(t)$ decreased to approximately 50 % of the control, whereas at 44.4 μg/ml, $\bar{I}(t)$ decreased to to an intensity only twice the background level.

Figure 4.8 shows a plot of $\bar{I}(t)$ against time for a control and the three concentrations of rOPN. The lowest concentration of rOPN, 1.14 μg/ml, gave a scattering intensity similar to the control measurement, which had the greatest scattered intensity of all the measurements. The middle concentration, 4.55 μg/ml, resulted in the greatest reduction in scattered intensity, while the highest concentration, 9.09 μg/ml, resulted in a relative increase in scattered

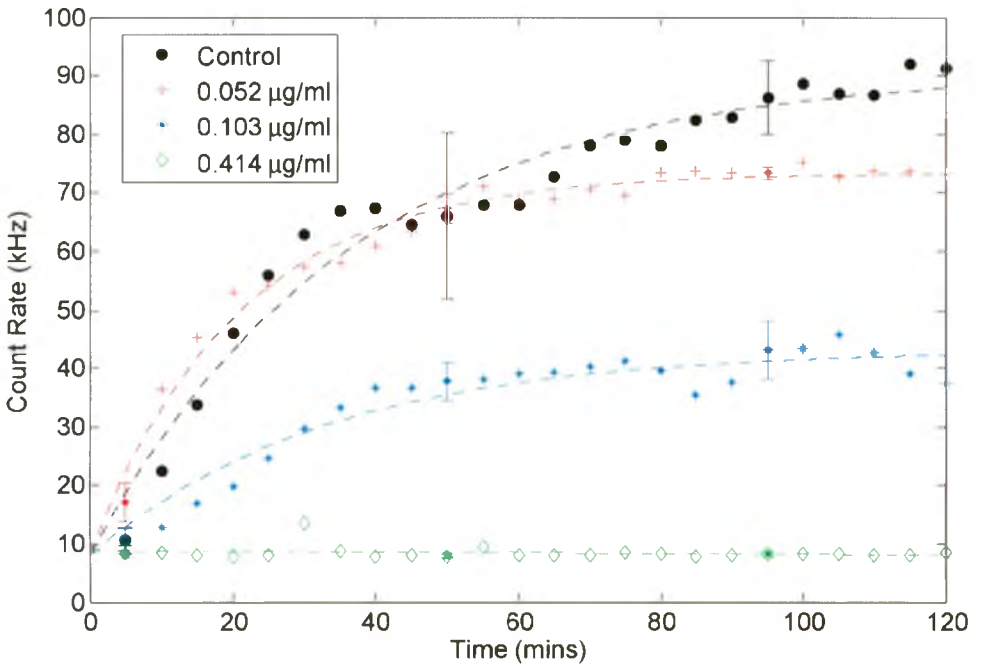

Figure 4.5: Count Rate in the presence of nOPN vs. Time

The five minute average count rate vs time for nOPN.

intensity over the 4.55 μg/ml measurement. The results from these experiments will be discussed further in terms of crystal inhibition in Chapter 5.

Autocorrelation Functions

An early gauge of the behaviour of the precipitate in solution is provided by the autocorrelation function, which is displayed in real time. Figure 4.9 shows the shifted intensity autocorrelation functions, $g^2(\tau) - 1$, from measurements using the highest concentration of rOPN at five, 55 and 110 minutes into the experiment. As the precipitation proceeds, the measurements become less noisy and $g^2(\tau) - 1$ decays more rapidly to zero. At early times, $I(t)$ is increasing on average, as seen in Figure 4.8. As a result, $I(t + \tau)$ is always

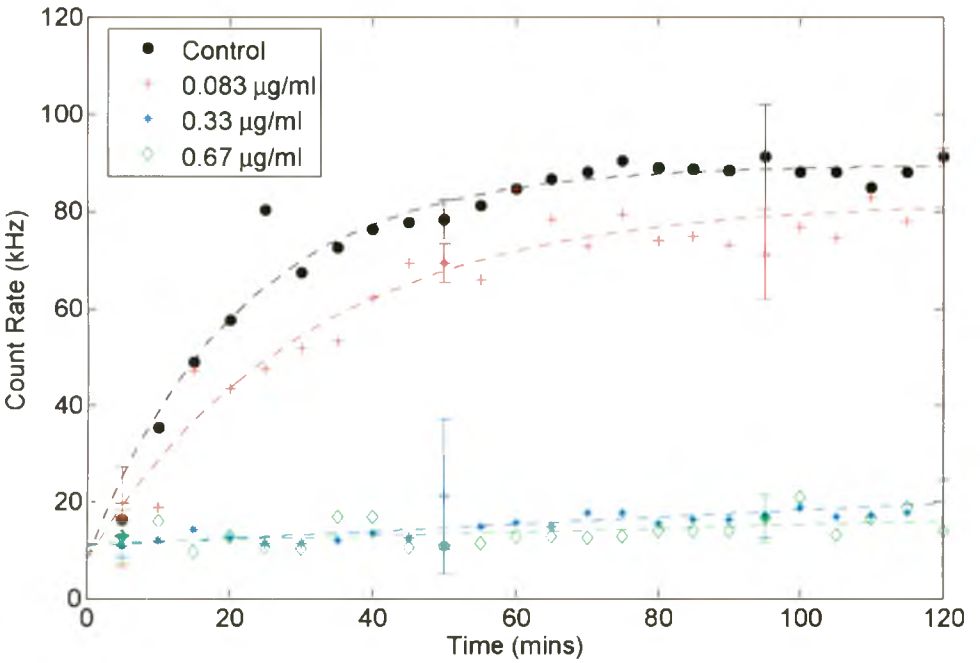

Figure 4.6: Count Rate in the presence of Poly-Asp vs. Time

The five minute average count rate vs time for poly-Asp.

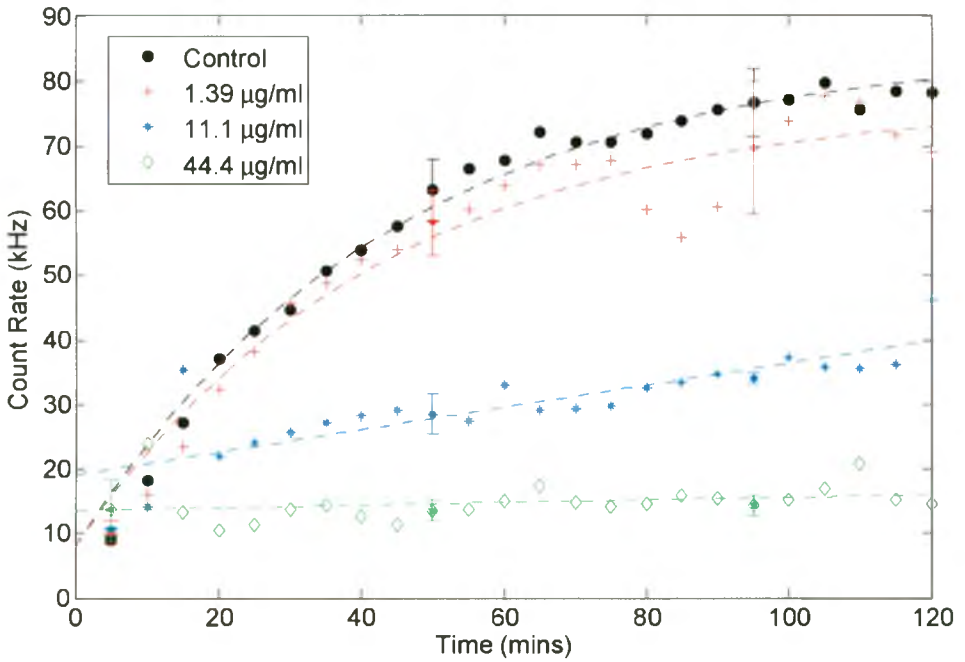

Figure 4.7: Count Rate in the presence of pOPAR vs. Time

The five minute average count rate vs time for pOPAR.

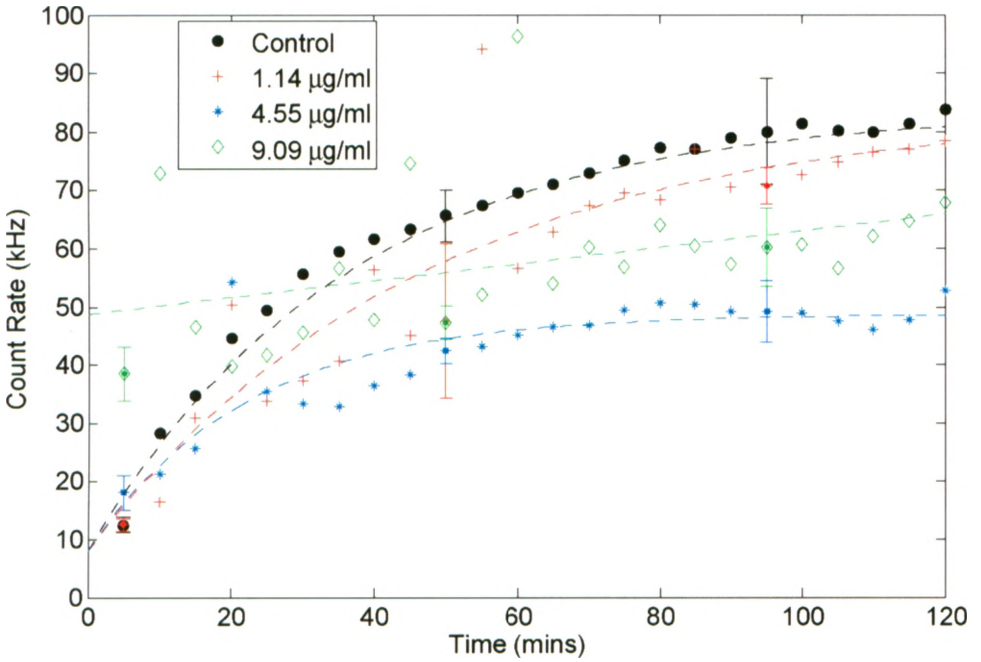

Figure 4.8: Count Rate in the presence of rOPN vs. Time

The five minute average count rate vs time for rOPN.

bigger than $I(t)$ on average, so $I(t+\tau)$ remains correlated with $I(t)$ even when τ gets large. For this reason, $g^2(\tau) - 1$ does not go to zero at long τ.

Plots of $g^2(\tau) - 1$ recorded 100 minutes into a control measurement, and measurements with the three concentrations of pOPAR are shown in Figure 4.10. This figure shows the importance of a strong scattered intensity to the correlation function. If a sample only scatters slightly more than the background levels, then $g^2(\tau) - 1$ is very noisy, as in the case of the highest concentration of pOPAR. A faster decay of the autocorrelation function results from smaller scattering particles. From the decay times of the functions plotted in Figure 4.10, we see that the particles precipitating at the highest pOPAR concentration are the smallest of the four, followed roughly by the control, the lowest concentration and the middle concentration of peptide.

Distribution Functions

From the decay of the autocorrelation functions, the computer software calculates the mean hydrodynamic radius, $\bar{r}$ of the scatterers and the distribution $P(r)$ of scatterer sizes.

Figure 4.11 is a plot of the four size distribution functions for a control measurement at 30, 60, 90 and 120 minutes. This figure shows a well defined distribution of mineral precipitants spanning roughly one order of magnitude in radius and increasing in size over time. At 30 minutes, the distribution shows a mean radius of about 100 nm, growing to about 300 nm by 120 minutes. This figure shows that the whole population of particles grows in time as a group.

$P(r)$ for 9.09 μg/ml rOPN at 30, 60, 90 and 120 minutes is plotted in Figure 4.12. At 30 minutes, $P(r)$ shows a broad size distribution, including

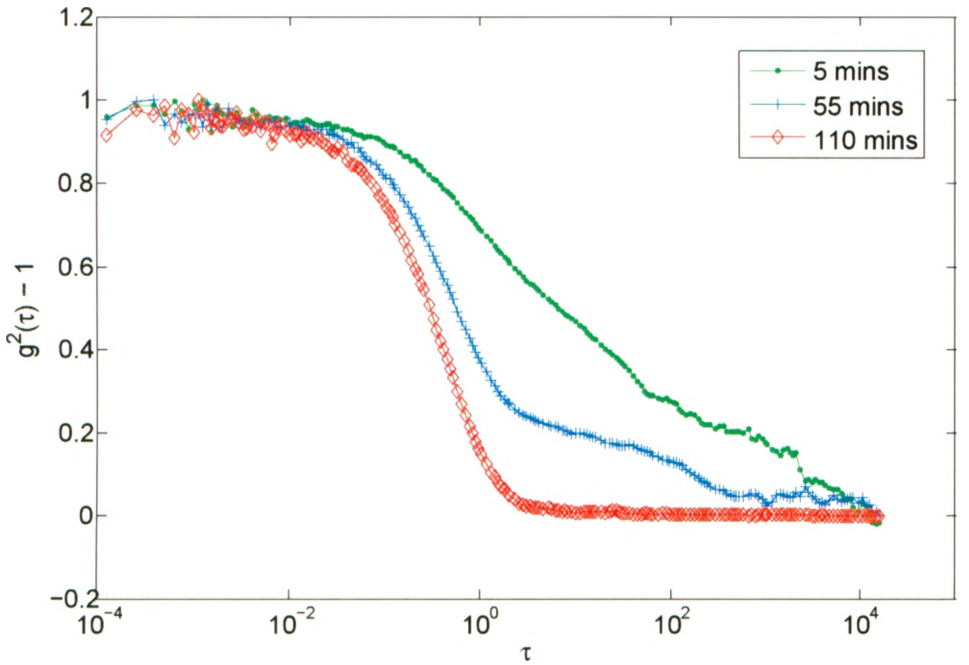

Figure 4.9: rOPN Autocorrelation Functions

The intensity autocorrelation function $g^2(\tau) - 1$ plots for 9.09 μg/ml rOPN at 5, 55 and 110 minutes into the experiment.

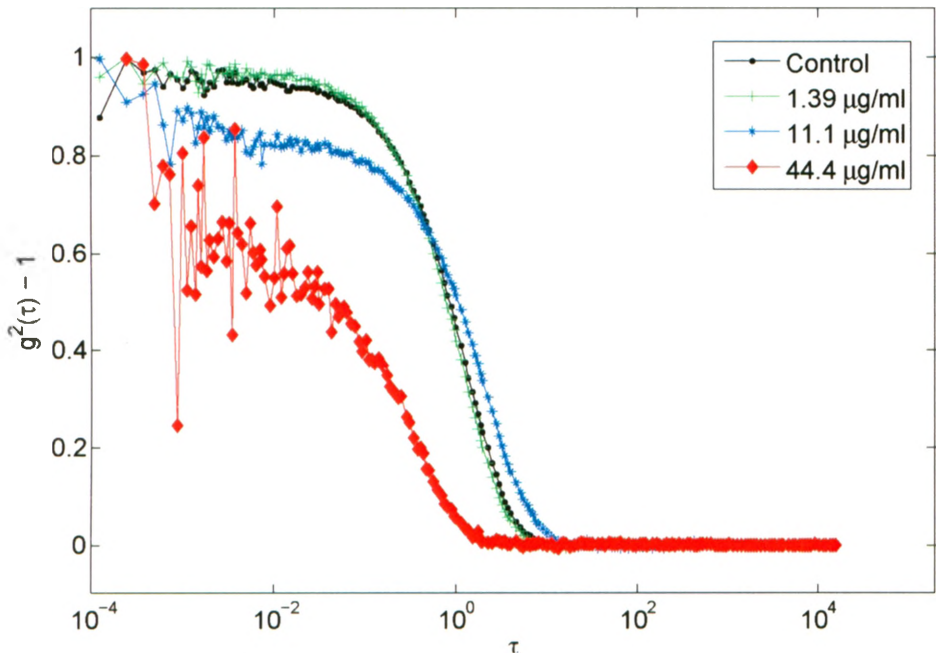

Figure 4.10: pOPAR Autocorrelation Functions

$g^2(\tau) - 1$ for a control and the three concentrations of pOPAR, 100 minutes into the measurements.

several peaks — one ranging from 20 to 200 nm with a mean of roughly 70 nm, a small peak at 450 nm, and another at 3500 nm. At 60 and 90 minutes, $P(r)$ has similarly distributed peaks, but the peak at smaller radii becomes weaker, while the peak of the largest radii becomes larger. At 120 minutes, $P(r)$ has a weak and relatively narrow peak centered on a radius of about 50 nm and a large peak at the end of the range corresponding to a radius of several microns. However, $I(t)$ scales with the sixth power of radius, and the scattered intensity is not particularly high, so it is very unlikely that the sample actually contains particles ≥ 3 microns in radius considering the results in Figure 4.8. Rather, the peaks at large r are likely a result of the noisy data.

$P(r)$ for 0.67 μg/ml poly-asp is plotted in Figure 4.13 at 30, 60, 90, and 120 minutes. At 30 minutes, $P(r)$ is very broad, spanning more than three orders of magnitude in r, with an additional peak at several microns. This distribution becomes progressively more narrow, with an average radius of 30 to 40 nm, as time progresses. At 120 min, $P(r)$ has a small peak corresponding to sub-nanometer particles, a large peak at about 40 nm and a very broad peak around 2500 nm. Figure 4.6 shows that the scattered intensity at this concentration of poly-asp was only slightly greater than background levels, so $g^2(\tau)$ was very noisy throughout the experiment. The sub-nanometer and the micron peaks are likely artifacts of the noisy data.

Average Measured Radius

A more accurate way to observe the growth of the precipitate is to look at the mean hydrodynamic radius, $\bar{r}$ as a function of time. Since the software saves $\bar{r}$ every five minutes for the duration of the measurement, we can plot the average radius against time to compare growth rates and precipitate sizes

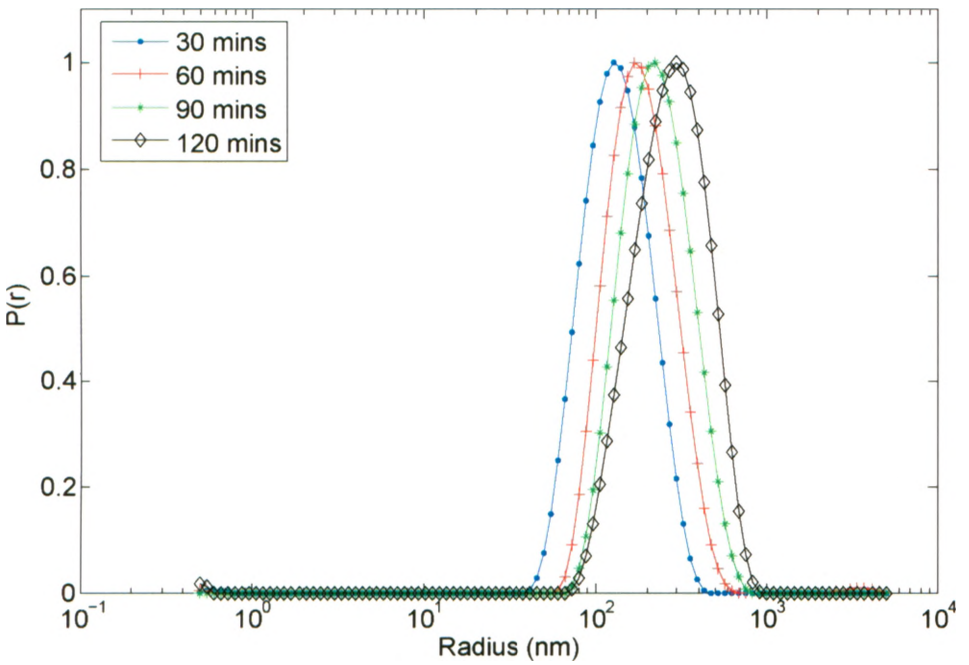

Figure 4.11: Size Distribution Functions for a Control Measurement

A plot of the distribution $P(r)$ of the radius r of the scatterers for a control measurement at 30, 60, 90, and 120 minutes. $P(r)$ is scaled so that its peak is at 1.

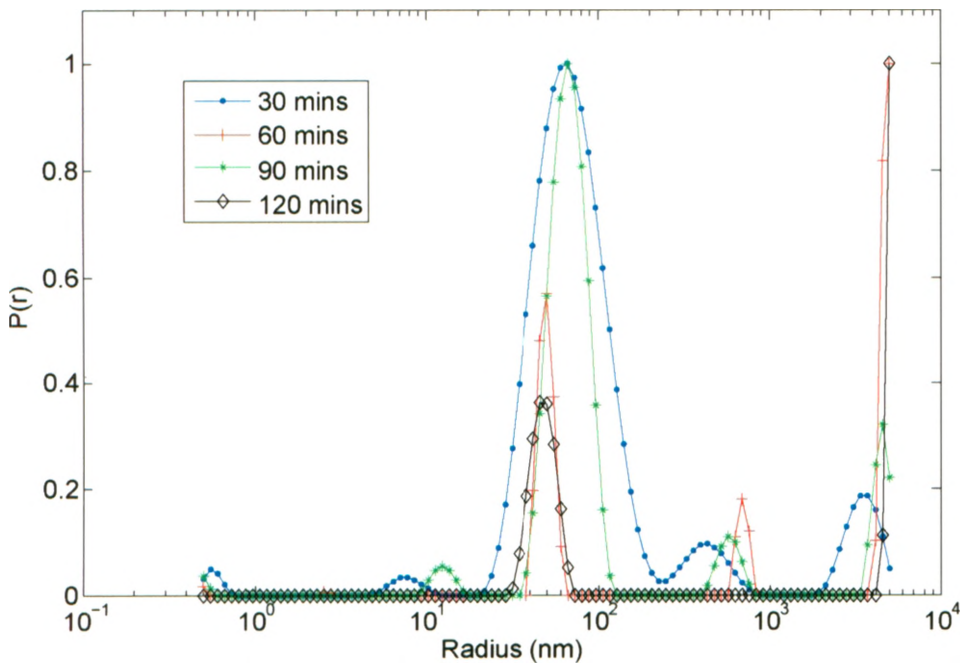

Figure 4.12: rOPN Size Distribution Functions

A plot of the distribution $P(r)$ of the radius r of the scatterers for 9.09 μg/ml of rOPN at times 30, 60, 90, and 120 minutes. $P(r)$ is scaled so that its peak is at 1.

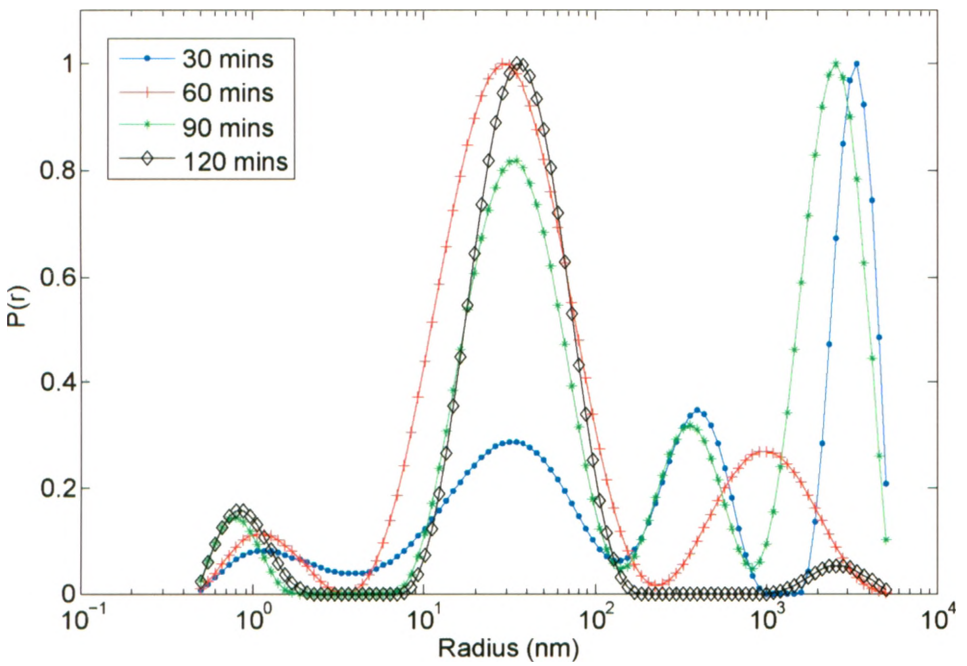

Figure 4.13: Poly-asp Size Distribution Functions

A plot of the distribution $P(r)$ of the radius r of the scatterers for 0.67 μg/ml of poly-asp at times 30, 60, 90, and 120 minutes. $P(r)$ is scaled so that its peak is at 1.

in a straightforward way.

$\bar{r}$ is plotted against time for the three concentrations of nOPN and a typical control measurement in Figure 4.14. The lowest concentration of nOPN yielded the largest and fastest growing crystals, followed by the middle concentration and the control measurement. The highest nOPN concentration gave virtually no precipitation or growth.

Figure 4.15 is a plot of $\bar{r}$ against time for a typical control measurement and the two lowest concentrations of poly-asp. The lowest concentration resulted in a population of crystals statistically similar to the crystals growing in the control experiment, and these two runs had the fastest growing populations. It does appear, however, that the two runs were becoming different at later times, where the crystals in the run with the lowest concentration of the peptide might have eventually become larger than those in the control. The middle concentration of poly-asp studied resulted in a population of crystals drastically reduced in size and growth rate compared to the control measurement. The greatest concentration of poly-asp had a scattered intensity close to background level and too noisy to allow for accurate radius measurements. A similar problem has been experienced by Harris *et al.* [57], who observed that although an increase in scattering was measured, the weak scattering signal precluded quantitative analysis of their data.

$\bar{r}$ is plotted against time for the two lowest concentrations of pOPAR and a control measurement in Figure 4.16. The lowest concentration of pOPAR had no measurable effect on the size or rate of growth of the crystals compared to the control measurement. The middle concentration studied resulted in much larger crystals growing at a much faster rate than the control measurement, while accurate radius measurements could not be obtained with the greatest concentration.

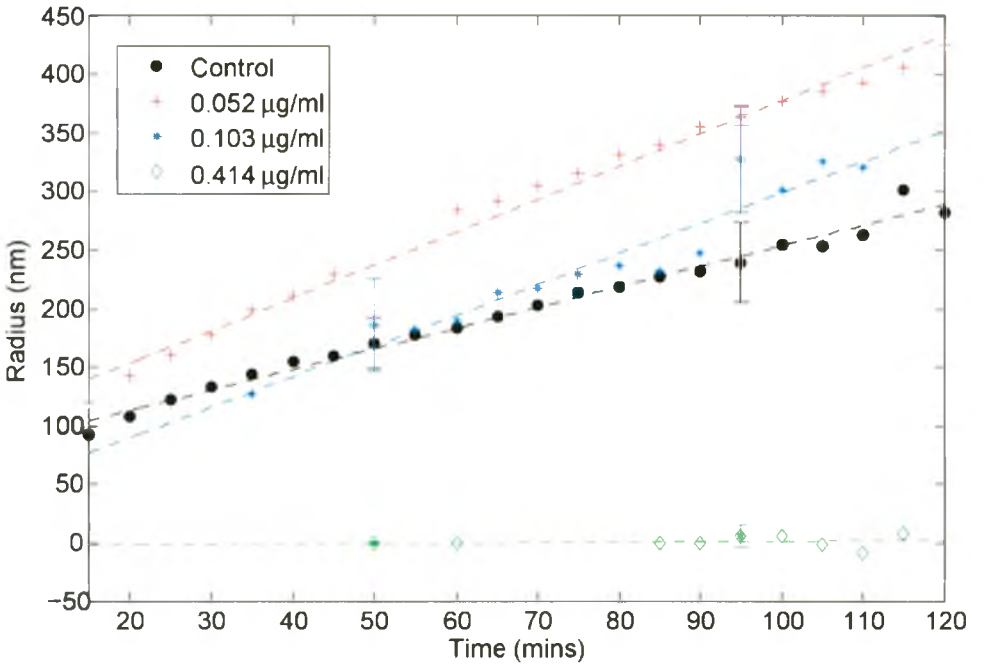

Figure 4.14: Precipitate $\bar{r}$ in nOPN Solution vs. Time

$\bar{r}$ versus time for nOPN solutions.

Figure 4.17 is a plot of $\bar{r}$ as a function of time for a typical control measurement and the two lowest concentrations of rOPN. The control experiment had the largest and fastest growing crystals by a wide margin. The lowest concentration of rOPN resulted in much smaller crystals than the control, and a growth rate of almost zero. The middle concentration resulted in even smaller crystals and a growth rate very close to zero. The highest concentration did not allow for accurate radius measurements. While the scattered intensity was well above background levels, $I(t)$ was very noisy which resulted in noisy autocorrelation functions and unreliable radius measurements. A possible reason for the noisy data in this case will be discussed in Chapter 5.

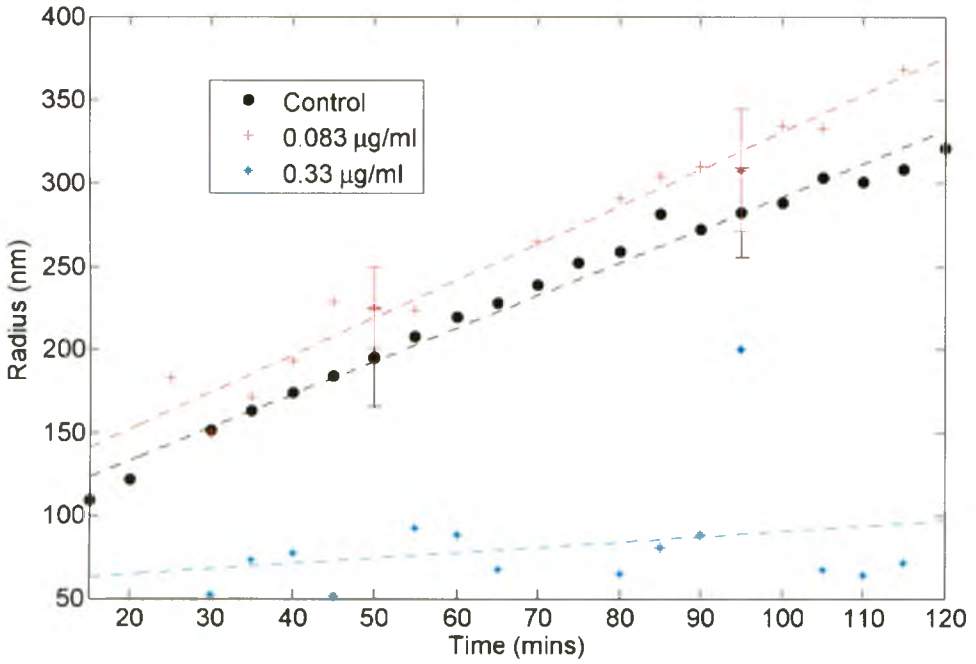

Figure 4.15: Precipitate $\bar{r}$ in Poly-Asp vs. Time

$\bar{r}$ versus time for poly-Asp solutions.

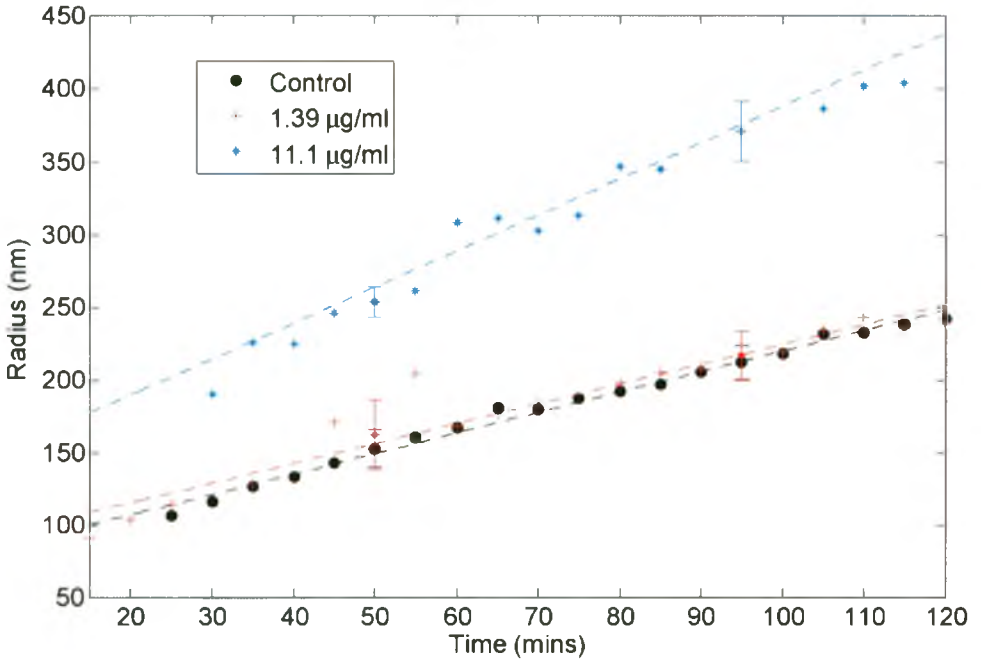

Figure 4.16: Precipitate $\bar{r}$ in pOPAR vs. Time

$\bar{r}$ versus time for pOPAR solutions.

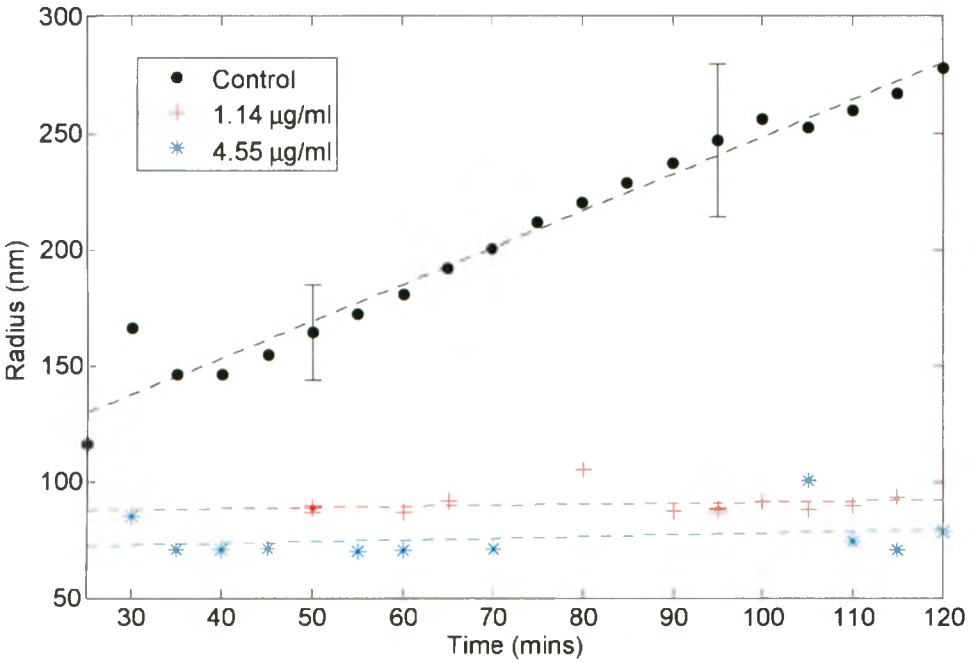

Figure 4.17: Precipitate $\bar{r}$ in rOPN vs. Time

$\bar{r}$ versus time for rOPN solutions.

Chapter 5

Discussion

Dynamic light scattering is becoming an increasingly common tool in the field of biomineral science. Since it is responsive to scatterers on the order of nanometers, is completely non-invasive, and measures sizes in real time, it is an excellent tool for certain experiments. It has been used to measure the sizes of suspended particles [62, 63, 75], induction time, that is, the lag time before crystal nucleation begins [76] and protein behaviour under different ionic conditions [77, 78]. In addition to giving the mean hydrodynamic radius, light scattering can provide the size distribution of the particles in real time. As such, dynamic light scattering can provide a meaningful assessment of protein-crystal interactions, particle populations, and growth rates.

Dynamic light scattering has its limitations. The calculated hydrodynamic radii are equal to the actual dimensions of the scatterers only if the scatterers are spheres, and as such, measurements on irregularly shaped objects will not provide information about the shapes. Light scattering also does not provide a direct measurement of the number of particles in solution nor can it characterize the precipitate. For this reason, it is common to use dynamic light

scattering in conjunction with other techniques including atomic force microscopy, x-ray diffraction, Raman spectroscopy, scanning/transmission electron microscopy or static light scattering (SLS). Nevertheless, previous studies using dynamic light scattering for measurements of calcium phosphate and hydroxyapatite precipitates have demonstrated the utility of the technique.

Jiang *et al.* [76] used dynamic light scattering to measure the induction time for hydroxyapatite nucleation in the presence and absence of the biomolecule chondroitin sulfate. X-ray diffraction was used to verify the presence of hydroxyapatite.

Onuma *et al.* [63] initially used atomic force microscopy to image a synthetic hydroxyapatite crystal face and measured step heights of 0.8 and 1.6 nm. This led to the assumption that the growth units of hydroxyapatite must be 0.8 nm in size. By using a modified dynamic light scattering system, they were able to measure stable calcium and phosphate clusters of 0.7 to 1.0 nm in diameter in simulated body fluid [63, 75]. Using two different solutions of Ca^{2+} and PO_4^{3-} they were able to confirm by dynamic light scattering that the clusters they had measured were in fact the growth units of hydroxyapatite and amorphous calcium phosphate (ACP). From their observations, Onuma *et al.* developed two models for hydroxyapatite formation [62]. The first postulates that ACP clusters eventually undergo internal restructuring and become hydroxyapatite, while the second model proposes that the amorphous cluster acts as a site of heterogeneous nucleation for hydroxyapatite, which grows over the ACP [62]. This group has used SLS, transmission electron microscopy and Raman spectroscopy to observe a transformation from amorphous to crystalline calcium phosphate facilitated by synthetic proteins. Using static light scattering, they measured the molecular weight, radius of gyration, and fractal dimension of the amorphous calcium phosphate in the presence or

absence of the proteins. Specifically, they were able to conclude that a transition from ACP to hydroxyapatite was accompanied by a change in molecular weight and fractal dimension, while the radius of gyration remained constant at approximately 340 nm. They confirmed this with Raman spectroscopy and transmission electron microscopy [79].

Heiss *et al.* [80] used dynamic light scattering to study protein mediated inhibition of calcium phosphate precipitation. They demonstrated that the protein α_2-HS glycoprotein/fetuin-A acted to inhibit the precipitation of calcium phosphate crystals, however at the maximum protein concentration, particles 30 to 150 nm in radius still formed. Using electron microscopy and dynamic light scattering measurements of the protein itself, Heiss *et al.* [80] proposed that the protein inhibits precipitation by encapsulating itself with apatite growth units into a soluble complex, instead of precipitating as an insoluble salt.

The goal of our study was to develop dynamic light scattering as a tool to study protein-mediated mineral formation. As demonstrated here, dynamic light scattering can be used to assess the effectiveness of inhibitors of hydroxyapatite crystallization. The results from Chapter 4 will now be discussed to compare the effects of each peptide on mineral nucleation and crystal growth. It is important to note, however, that hydroxyapatite crystals are not spherical, so the measured hydrodynamic radii can only be taken as an indication of the average particle dimensions. Although amorphous calcium phosphate is spherical [81], hydroxyapatite crystals are generally needle- and plate-like in shape [11], in bone the dimensions of which are approximately 35-40 $\times$ 10-20 $\times$ 2.5-5 nm [12] (synthetic crystals, however, can be grown much larger [82,83]). The fact remains though that we have been able to measure linear growth of the precipitate and these results are enlightening and complementary to the

other information determined by dynamic light scattering.

The nOPN strongly inhibited crystal growth. At 0.414 μg/ml, the greatest concentration tested, the scattered intensity did not increase above the background and the measured particle radius was essentially zero at all times. At this concentration, nOPN appears to have completely prevented nucleation, and there was no growth to measure. At 0.103 μg/ml the scattering intensity was reduced by roughly 50% compared to the control measurement. In this case, the radius measurements indicated that the crystals that did form were larger and faster growing than in the control experiment. Since the scattered intensity increases vary rapidly with particle radius, the large radius and relatively low scattered intensity, indicates that there must be far fewer particles suspended in the solution than in the control. This behaviour is likely due to the solution containing insufficient protein to completely inhibit nucleation. The small population of nuclei that did form was able to grow faster than in the control experiments because their smaller number meant that there was less competition for the free ions in solution. At 0.052 μg/ml, a similar phenomenon was observed. In both cases the slope of the radius vs. time graph was greater than 2 nm/min, which is larger than the average growth rate for all the control measurements, which was 1.65 nm/min. In this case, however, the crystals did not grow as large or as quickly, and the scattering intensity was only slightly lower than the control experiment. This suggests that at the lowest protein concentration, some nucleation was prevented, but less than at 0.103 μg/ml. As a result there were more particles nucleated, more competition for ions, and so smaller particles and lower growth rates.

Poly(aspartic acid) was also a strong inhibitor, with our measurements showing almost no increase in $\bar{I}(t)$ at a concentration of 0.67 μg/ml. Radius measurements could not be made at this concentration, but based on the low

scattering intensity it is likely that very little nucleation occurred. At a poly-asp concentration of 0.33 μg/ml, some crystal growth was observed. Compared to control measurements, there was a significant decrease in $\bar{I}(t)$ and the hydrodynamic radii and growth rates measured at this concentration were well below those of the control measurements, with a measured growth rate of less than 1.0 nm/min. This behaviour appears consistent with previous work, which indicated that poly-asp binds with high affinity to hydroxyapatite [30], rendering growth difficult for those nuclei that do form. At the lowest concentration of poly-asp studied, $\bar{I}(t)$ was slightly lower than the control experiments, with the resulting particles having radii statistically similar to those in the control measurement. This suggests that a slightly smaller population of calcium phosphate particles than in the control experiment was able to be nucleated and grew with minimal restriction.

Phosphorylated OPAR also inhibited hydroxyapatite growth but required a concentration more than four times greater than any other proteins or peptides studied to achieve almost complete inhibition. pOPAR exhibited behaviour very similar to nOPN. At the highest concentration, pOPAR gave an almost constant scattered intensity only slightly higher than the background. While particle radii could not be determined for this experiment, the creeping increase in the intensity suggests that some particles were nucleating, albeit very slowly. At 11.1 μg/ml, the scattering intensity was reduced by approximately 50% below the control, and the crystals were larger and faster growing, with a growth rate of greater than 2 nm/min, similar to what was observed in the experiments with nOPN. As with nOPN and poly-asp, the behaviour observed suggests that a small population of crystals nucleated and grew rapidly in the ion-rich solution. The lowest concentration studied had no measurable effect on either the scattering intensity or the radius.

rOPN did not appear to have any effect on crystal nucleation. At 9.09 μg/ml there was actually an increase in the scattered intensity over the 4.55 μg/ml measurement. This behaviour can perhaps be explained by protein-protein interactions and protein oligomerization occurring as a result of the high protein concentration. OPN polymerization has in fact been observed by others [77]. The highest concentration of rOPN experiments were very noisy, which prevented accurate measurements of radii. It is possible that protein-protein interactions are responsible for this noise. At 4.55 μg/ml, the scattering intensity was about 40% below the control measurement, with measured radii indicative of much smaller particles. At 1.14 μg/ml the scattered intensity was only slightly lower than the control measurement, but the measured radius was still much smaller than in the control experiment. This is indicative of a large number of very small particles. Furthermore, since the calculated growth rates were low, less than 0.1 nm/min, but the scattering intensity was virtually unchanged, it appears as though rOPN binds to crystals after they nucleate and restricts further growth.

Figure 5.1 is a plot of the crystal growth rates from each experiment, determined from the slope of the radius versus time graphs shown in Chapter 4, plotted against concentration for each protein or peptide. In the cases where the crystal radii could not be measured, growth rates have been assumed to be zero. The black line is the average growth rate from all the control measurements. Figure 5.1 illustrates that the behaviour of pOPAR is different from that of the other three inhibitors, in that it requires far greater concentrations for complete inhibition of nucleation or growth. rOPN effectively restrains crystal growth and looks as though it might fall on a common curve with nOPN and poly-asp, both of which demonstrate strong inhibitory potency for nucleation and growth.

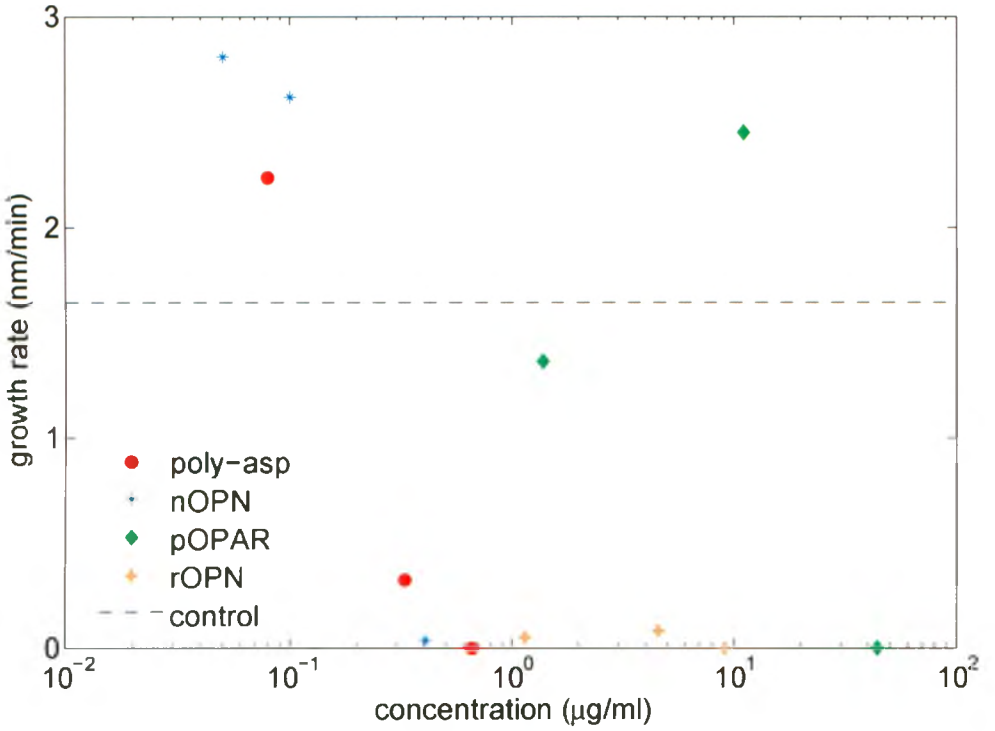

Figure 5.1: Growth Rate vs. Concentration

A growth rate vs concentration plot comparing the growth rates for each concentration of protein/peptide we studied.

The concentrations required to inhibit crystal growth in our experiments are consistent with those found in inhibition experiments using the constant composition [72] and auto-titration methods described in Chapter 1 [24,44,52]. The results from these experiments and several others are listed in Table 5.1. For both the constant composition and auto-titration methods, it is common to record inhibitory potency in terms of the so-called IC_{50} value. This is the concentration required to achieve an inhibition of nucleation or growth of 50% compared to the control measurement. These studies are not necessarily directly comparable. In three of the constant composition and auto-titration studies [44,52,72], inhibition of the growth of seed crystals (hydroxyapatite) in a calcium phosphate solution was being measured, while in the present study and one of the auto-titration studies [24], inhibition of particle nucleation and early growth was measured. It is also important to note that Azzopardi [72] used milk OPN, which has approximately 30 phosphorylations, while nOPN has 10. In two cases, [44, 52] dephosphorylated nOPN was used instead of rOPN, which was missing most but not all of its phosphorylations. For our purposes, the IC_{50} values will be compared with estimated values of the concentration that would give a 50% reduction in scattering intensity for each protein or peptide we studied. Azzopardi [72] gives values for complete inhibition, so our highest concentrations are listed as well, although it is possible that complete inhibition could be achieved at lower concentrations.

Table 5.1 shows that our results are in reasonable agreement with other previous work. Our estimated IC_{50} values are slightly higher than those found by Hunter *et al* [44] and Goldberg *et al* [52] and slightly lower than those found by Hunter *et al.* [24] and Azzopardi [72] with the exception of pOPAR. In our case the required concentration of pOPAR was roughly six times greater than that found by Azzopardi [72].

Table 5.1: Comparison with Previous Work

	OPN μg/ml	rOPN μg/ml	poly-asp μg/ml	pOPAR μg/ml
[44, 52] IC_{50}	0.06	> 4	0.11	N/A
[24] IC_{50}	0.32	N/A	N/A	N/A
[72] IC_{50}	1.94	5.23	1.45	1.65
This work IC_{50}	≈ 0.103	$\approx$ 4.0-5.0	≈ 0.2	≈ 11.1
[72] IC_{100}	4.6	> 13	5.5	7.4
This work IC_{100}	< 0.414	> 9.09	< 0.67	< 44.4

This table shows the concentrations required to achieve 50% and 100% inhibition of growth of hydroxyapatite seed crystals along with the results from our studies.

Table 5.2: Reagent Inhibitor Qualities

	Length (amino acids)	Aspartic Acids	Phosphorylations	Flexible
nOPN	301	42	10	yes
rOPN	301	42	0	yes
poly-asp	95	95	0	yes
pOPAR	16	11	1	yes

Characteristics of the proteins and peptides used in this study.

A number of molecular properties believed to be associated with good inhibitors were discussed in Section 1.3, including the number of charged residues, and in particular, the number of aspartic and glutamic acid residues [30], the number of phosphorylations [25] and flexibility or lack of secondary structure [30]. These qualities are summarized in Table 5.2 for the proteins and peptides used in this study.

Comparing the results obtained with nOPN, which we found to strongly inhibit hydroxyapatite nucleation, and rOPN, which was much less effective, suggests that phosphorylations increase the ability of OPN to inhibit nucleation. They do not, however, appear to be required for the prevention of growth, since the poly-asp peptide contains no attached phosphates and nonetheless was almost as potent as nOPN at inhibiting nucleation and was very good at slowing the growth rate of crystals that did form. However, while rOPN was the least effective inhibitor of nucleation, it was a very potent inhibitor of crystal growth after nucleation occurred. This is significant, as none of the other assays used in our lab have been able to demonstrate this phenomenon. In fact, depending on the assay system, recombinant OPN is viewed as a rather poor inhibitor [44], or even a protein with no inhibitory activity [46]. Finally, pOPAR, a representative peptide from the nOPN polypeptide sequence, required about 100 times the concentration by mass, and approximately 2000 times by molar concentration, to inhibit nucleation and growth at levels comparable to nOPN. This suggests that length plays a critical role in the ability of peptides or proteins to inhibit nucleation. nOPN has 301 residues, while the synthetic pOPAR contains only 16. While they are both highly negatively charged and include phosphorylations and aspartic acids, pOPAR is much less potent than nOPN. The primary difference between them is their length. As discussed in [72] and Section 1.3.1, a long and flexible protein could prevent nu-

cleation by enveloping a sub-critical nucleus, and preventing it from achieving the critical radius.

The highest concentrations of nOPN, poly-asp and pOPAR succeeded in inhibiting virtually all precipitation of calcium phosphate. Lower concentrations of these proteins and peptides and of rOPN appeared to alter the number and growth rates of the crystals that did precipitate. Characterization of the precipitate using additional experimental techniques would lead to a better understanding of the shapes and composition of our precipitates. In our experiments, however, visible product never precipitated out of solution, even after two months, which renders Raman or x-ray diffraction characterization difficult. Other techniques, such as electron microscopy, would require significant sample manipulations which could cause changes to the nature of the calcium phosphate precipitate. For example, ACP could be transformed into mineral crystal during the processing of the samples. On the other hand, static light scattering can provide information regarding the shapes of the particles [68], and estimates of the molecular weights, fractal dimensions, and radius of gyration [79]. It is possible to do such measurements with our light scattering system, although they may be difficult due to the small size of the particles and the fact that they are growing over time.

Static light scattering involves measuring the time averaged scattered intensity as a function of q. This is difficult when the system being studied is changing rapidly with time. Especially in the first 30 minutes of our experiments, the scattered intensity increased rapidly with time. Performing time-resolved measurements of the intensity at a sufficient number of scattering angles in this system would be very difficult. Onuma *et al.* [62] overcame this difficulty by focusing an ellipsoidal mirror onto a high-speed CCD camera in such a way that they could measure the intensity at angles from 10° to 170°

virtually simultaneously, with an angular resolution of 0.6°. With this system they were able to perform time resolved static light scattering measurements on a rapidly evolving system. Although it would likely be difficult, trying to do SLS measurements on our system could be worthwhile.

In summary, nOPN, poly-asp and pOPAR have been demonstrated to be effective inhibitors of hydroxyapatite nucleation, albeit at much different concentrations. rOPN has been shown to strongly restrict crystal growth after nucleation has occurred. The results of this study suggest that phosphorylations on osteopontin are an important contributor to nucleation inhibitor potency, but they are not necessarily essential for affecting growth. It appears that length may also be an important factor in the ability of a protein or peptide to inhibit nucleation. We have also demonstrated that dynamic light scattering provides a fast and reliable method of assessing inhibitory potency and provides information that is not readily available by other means, including growth rates and crystal sizes in real time. While characterization of the precipitation product, or determination of the shape of the precipitating crystals was beyond the scope of this project, these are issues that could be addressed in future work.

Chapter 6

Conclusions and Future Directions

6.1 Conclusions

Dynamic light scattering provides a wealth of information. Beyond simply measuring particle radii, it is possible to determine growth rates, to estimate relative population sizes, and to make informed guesses about protein-crystal interactions. Until this work, rOPN has been widely regarded as a poor inhibitor. While we have demonstrated that rOPN plays no significant role in the inhibition of the initial nucleation of mineral crystals, it appears to be a potent inhibitor of subsequent crystal growth, decreasing particle growth rates almost to zero.

We found that radius measurements alone can be misleading. In some of our experiments, the radius measurements and growth rates would appear to indicate that the protein or peptide actually encouraged precipitate growth. Conversely, looking at the radius measurements alone would make rOPN ap-

pear to be the best inhibitor. When the average scattered intensity is considered as well, though, the interpretation of the behaviour of these solutions becomes much different. The radius measurements alone would suggest that small populations of particles formed stable nuclei and quickly grew in the ion-rich environment, while in the case of rOPN, it appears that large populations of particles nucleated, but were then severely restricted in their growth. This behaviour of rOPN may serve a purpose similar to what Heiss *et al.* [80] have proposed for α_2-HS glycoprotein/fetuin-A. They suggested that α_2-HS glycoprotein/fetuin-A binds and encases itself in hydroxyapatite growth clusters, keeping the mineral soluble so that the body can flush it away before it precipitates. Perhaps rOPN serves a similar function, binding apatite before it precipitates, preventing it from depositing and providing the body with an opportunity to flush it away.

The results we obtained in this work using dynamic light scattering are, in general, in line with previous studies. Furthermore, we have demonstrated that rOPN is a potent inhibitor of crystal growth, which was not known previously. While we have successfully confirmed a broad and potentially powerful role for dynamic light scattering in biomineralization science with regards to assessing protein interactions with crystals, we have also revealed a number of questions that could be addressed in future work.

6.2 Future Directions

The two proteins and two peptides used in this experiment were useful in demonstrating the utility and effectiveness of dynamic light scattering in assessing the potency of inhibitor proteins on hydroxyapatite growth. The differences between the four molecules are too numerous to allow any claims as to

which properties are necessary for a good inhibitor, however. While it does appear that a longer peptide with attached phosphates would be optimal, there are distinct advantages to using smaller peptides in generating therapeutics for the prevention of pathological calcification. It would therefore be useful to investigate several different properties in greater detail, including the role of peptide length in the inhibition process, the role of secondary structure, and the quantity and distribution of specific acidic residues in proteins. Atomic force microscopy measurements have shown that ions such as Mg^{2+} and Zn^{2+} inhibit the growth of larger hydroxyapatite crystal faces by adsorbing to kink sites [84], while other ions such as F^- and Pb^{2+} readily incorporate themselves into the crystal structure of bone [12,29]. Since true bone actually contains a number of elemental impurities, it would be relevant to study hydroxyapatite growth in the presence of ionic impurities to determine their effects on growth rates and nucleation.

Tarasevich *et al.* [85] have demonstrated the ability of amelogenin to enhance calcium phosphate nucleation by measuring nucleation induction time with a quartz crystal microbalance, while Jiang *et al.* [76] used dynamic light scattering to measure the nucleation induction time of chondroitin sulfate. It would be enlightening to apply our system to potential nucleators of hydroxyapatite growth. Bone sialoprotein has been shown to be a potent nucleator of hydroxyapatite [22], and it would be of great interest to observe that behaviour with dynamic light scattering.

Finally, there are several drawbacks of dynamic light scattering that could be at least partially addressed by establishing a static light scattering protocol as well. Perhaps after the first thirty minutes of rapidly increasing scattered intensity, it would be possible to make several brief measurements at different scattering vectors in a period of several minutes. Such a protocol would require

optimization, but it could be possible to establish estimates for the shapes of the particles. In doing so, it might then be possible to distinguish between amorphous and crystal calcium phosphate.

Bibliography

[1] Weiner, S., and Dove, P. M. (2003) An overview of biomineralization processes and the problem of the vital effect. Reviews in Mineralogy and Geochemistry **54**, 1–29

[2] Knoll, A. H. (2003) Biomineralization and evolutionary history. Reviews in Mineralogy and Geochemistry **54**, 329–356

[3] Addadi, L., Joester, D., Nudelman, F. and Weiner, S. (2006) Mollusk shell formation: a source of new concepts for understanding biomineralization porocesses. Chemistry — A European Journal **12**, 980–987

[4] Mann, S. *Biomineralization; principles and concepts in bioinorganic materials chemistry* (Oxford University Press, New York, 2001)

[5] Webb. M. A. (1999) Cell-mediated crystallization of calcium oxalate in plants. Plant Cell **11**, 751–761

[6] Currey, J. D. (1999) The design of mineralised hard tissues for their mechanical functions. Journal of Experimental Biology **202**, 3285–3294

[7] Addadi, L. and Weiner, S. (1985) Interactions between acidic proteins and crystals: stereochemical requirements for biomineralization. Proceedings of the National Academy of Sciences **82**, 4110–4114

[8] Wetherbee, R. (2002) The diatom glasshouse. Science **298**, 547

[9] Lowenstam, H. A. (1981) Minerals formed by organisms. Science **211**, 1126–1131

[10] Mann, S. (1983) Mineralization in biological systems. Structure and Bonding **54**, 125–174

[11] Francillon-Vieillot, H., de Buffrénil, V., Castanet, J., Géraudie, J., Meunier, F. J., Sire, J. Y., Zylberberg, L. and de Ricqlès, A. in Carter, J. G. ed. *Skeletal biomineralization: patterns, processes and evolutionary trends volume I* (Van Norstrand Reinhold, 1990)

[12] Posner, A. S. (1969) Crystal chemistry of bone mineral. Physiological Reviews **49**, 760–792

[13] Omelon, S. J., and Grynpas, M. D. (2008) Relationship between phosphate chemistry, biochemistry and apatite biomineralization. Chemical Reviews **108**, 4694–4717

[14] Holick, M. F. (2000) Microgravity-induced bone loss—will it limit human space exploration? The Lancet **355** 1569–1570

[15] http://www.kidney.ca/page.asp?intNodeID=22132

[16] Coe, F. L., Evan, A., and Worcester, E. (2005) Kidney stone disease. The Journal of Clinical Investigation **115**, 2598–2608

[17] Wada, T., McKee, M. D., Steitz, S. and Giachelli, C. M. (1999) Calcification of vascular smooth muscle cell cultures: inhibition by osteopontin. Circulation Research **84**, 166–178

[18] Johnson, R. C., Leopold, J. A., and Loscalzo, J. (2006) Vascular calcification pathobiological mechanisms and clinical implications. Circulation Research **99**, 1044–1059

[19] De Yoreo, J. J. and Vekilov, P. G. (2003) Principles of crystal nucleation and growth. Reviews in Minerology and Geochemistry **54**, 57–93

[20] Jackson, K. A., *Kinetic Processes, crystal growth diffusion, and phase transitions in materials* (Wiley-VCH, Weinheim, 2004)

[21] Veis, A. (2003) Mineralization in organic matrix frameworks. Reviews in Mineralogy and Geochemistry **54**, 249–289

[22] Hunter, G. K. and Goldberg, H. A. (1993) Nucleation of hydroxyapatite by bone sialoprotein. Proceedings of the National Academy of Sciences **90**, 8562–8565

[23] Tye, C. E., Rattray, K. R., Warner, K. J., Gordon, J. A. R., Sodek, J, Hunter, G. K. and Goldberg, H. A. (2003) Delineation of the hydroxyapatite-nucleating domains of bone sialoprotein. The Journal of Biological Chemistry **278**, 7949–7955

[24] Hunter, G. K., Hauschka, P. V., Poole, A. R., Rosenberg, L. C. and Goldberg, H. A. (1996) Nucleation and inhibition of hydroxyapatite formation by mineralized tissue proteins. Biochemical Journal **317**, 59–64

[25] Termine, J. D., Eanes, E. D., and Conn, K. M. (1980) Phosphoprotein modulation of apatite crystallization. Calcified Tissue International **31**, 247–251

[26] Fisher, L. W., Torchia, D. A., Fohr, B., Young, M. F., and Fedarko, N. S. (2001) Flexible Ssructures of SIBLING proteins, bone sialoprotein, and osteopontin. Biochemical and Biophysical Research Communications **280**, 460–465

[27] Gorski, J. P. (1992) Acidic phosphoproteins from bone matrix: a structural rationalization of their role in biomineralization. Calcified Tissue International **50**, 391–396

[28] Tye, C. E., Hunter, G. K., and Goldberg, H. A. (2005) Identification of the type I collagen-binding domain of bone sialoprotein and characterization of the mechanism of interaction. The Journal of Biological Chemistry **280**, 13487–13492

[29] Romberg, R. W., Werness, R. G., Riggs, B. L., and Mann, K. G. (1986) Inhibition of hydroxyapatite crystal growth by bone-specific and other calcium-binding proteins. Biochemistry **25**, 1176–1180

[30] Goldberg, H. A., Warner, K. J., Li, M. C., and Hunter, G. K. (2001) Binding of bone sialoprotein, osteopontin and synthetic polypeptides to hydroxyapatite. Connective Tissue Research **42**, 25–37

[31] Oldberg, A., Franzen, A., and Heinehard, D. (1988) The primary structure of cell-binding bone sialoprotein. The Journal of Biological Chemistry **263**, 19430–19432

[32] Butler, W. T. (1989) The nature and signifigance of osteopontin. Connective Tissue Research **23**, 123–136

[33] Gorski, J. P., Kremer, E., Ruiz-Perez, J., Wide, G. E., and Artigues, A. (1995) Conformational analysis on solouble and surface bound osteopontin. Annals of the New York Academy of Sciences **760**, 12–23

[34] Butler, W. T. (1995) Structural and functional domains of osteopontin. Annals of the New York Academy of Sciences **760**, 6–11

[35] Keykhosravani, M., Doherty-Kirby, A., Zhang, C., Brewer, D., Goldberg, H. A., Hunter, G. K., and Lajoie, G. (2005) Comprehensive identification of post-translational modifications of rat bone osteopontin by mass spectrometry. Biochemistry **44**, 6990–7003

[36] Sørenson, E. S., Højrup, P., and Petersen, T. E. (1995) Posttranslational modifications of bovine osteopontin: identification of twenty-eight phosphorylation and three O-glycosylation sites. Protein Science **4** 2040–2049

[37] Giachelli, C. M. and Steitz, S. (2000) Osteopontin: a versatile regulator of inflammation and biomineralization. Matrix Biology **19**, 615–622

[38] Denhardt, D. T. and Guo, X. (1993) Osteopontin: a protein with diverse functions. The Federation of American Societies for Experimental Biology Journal **7**, 1475–1482

[39] Brown, L. F., Berse, B., Van de Water, L., Papadopoulos-Sergiou, A., Perruzzi, C. A., Manseau, E. J., Dvorak, H. F. and Senger, D. R. (1992) Expression and distribution of osteopontin in human tissues: widespread association with luminal epithelial surfaces. Molecular Biology of the Cell **3**, 1169–1180

[40] Mazzali, M., Kipari, T., Ophascharoensuk, V., Wesson, J. A., Johnson, R. and Hughes, J. (2002) Osteopontin — a molecule for all seasons. Quarterly Journal of Medicice **95**, 3–13

[41] Boskey, A. L. (1995) Osteopontin and related phosphorylated sialoproteins: effects on mineralization. Annals of the New York Academy of Sciences **760**, 249–256

[42] Wang, L., Guan, X., Tang, R., Hoyer, J. R., Wierzbicki, A., De Yoreo, J. J., and Nancollas, G. H. (2008) Phosphorylation of osteopontin is required for inhibition of calcium oxalate crystallization. Journal of Physical Chemistry B **112**, 9151–9157

[43] Shiraga, H., Min, W., VanDusen, W. J., Clayman, M. D., Miner, D., Terrell, C. H., Sherbotie, J. R., Foreman, J. W., Przysiecki, C., Neilson, E. G. and et al. (1992) Inhibition of calcium oxalate crystal growth in vitro by uropontin: another member of the aspartic acid-rich protein superfamily. Proceedings of the National Acadedemy of Sciences **89**, 426–430

[44] Hunter, G. K., Kyle, C. L. and Goldberg, H. A. (1994) Modulation of crystal formation by bone phosphoproteins: structural specificity of the osteopontin-mediated inhibition of hydroxyapatite formation. Biochemical Journal **300**, 723–728

[45] Oldberg, A., Franzen, A., and Heinegard, D. (1986) Cloning and sequence analysis of rat bone sialoprotein (osteopontin) cDNA reveals an Arg-Gly-Asp cell binding sequence. Proceedings of the National Academy of Sciences. **83**, 8819–8823

[46] Gericke, A., Qin, C., Spevak, L., Fujimoto, Y., Butler, W. T., Sorensen, E. S., and Boskey, A. L. (2005) Importance of phosphorylation for osteopontin regulation of biomineralization. Calcified Tissue International **77**, 45–54

[47] Pampena, D. A., Robertson, K. A., Litvinova, O., Lajoie, G., Goldberg, H. A. and Hunter, G. K. (2004) Inhibition of hydroxyapatite formation by osteopontin phosphopeptides. Biochemical Journal **378**, 1083–1087

[48] Grohe, B., O'Young, J., Ionescu, A., Lajoie, G., Rogers, K .A., Karttunen, M., Goldberg, H. A. and Hunter, G. K. (2007) Control of calcium oxalate crystal growth by face-specific adsorption of an osteopontin phosphopeptide. Journal of the American Chemical Society **129**, 14946–14951

[49] Asplin, J. R., Arsenault, D., Parks, J. H., Coe, F. L. and Hoyer, J. R. (1998) Contribution of human uropontin to inhibition of calcium oxalate crystallization. Kidney International **53**, 194–199

[50] Hoyer, J. R., Otvos, L., and Urge, L. (1995) Osteopontin in urinary stone formation. Annals of the New York Academy of Sciences **760**, 257–265

[51] Boskey, A. L., Spevak, L., Pashalis, E., Doty, S. B., and McKee, M. D. (2002) Osteopontin deficiency increases mineral content and mineral crystallinity in mouse bone. Calcified Tissue International **71**, 145–154

[52] Goldberg, H. A. and Hunter, G. K. (1995) The inhibitory activity of osteopontin on hydroxyapatite formation *in vitro*. Annals of the New York Academy of Sciences **760**, 305–308

[53] Pusey, P. N. in Linder, P. and Zemb, T., eds. *Neutron, X-Rays and Light: Scattering Methods Applied to Soft Condensed Matter* (Elseivier, Amsterdam, 2002)

[54] Twomey, T. A. M., Mackay, M., Kuipers, H. P. C. E., and Thompson, R. W. (1994) In situ observation of silicalite nucleation and growth: a light-scattering study. Zeolites **14**, 162–168

[55] Singh, P. S., Dowling, T. L., Watson, J. N., and White, J. W. (1999) Light and x-ray scattering from the early growth stages of zeolite A part I. Physical Chemistry Chemistry Physics **1999**, 4125–4130

[56] Schoeman, B. J. (1997) A high temperature *in situ* laser light-scattering study of the initial stage in the crystallization of TPA-silicate-1. Zeolites **18**, 97–105

[57] Harris, D. R., Keir, R. I. Prestidge, C. A., and Thomas, J. C. (1999) A dynamic light scattering investigation of nucleation and growth in supersaturated alkaline sodium aluminate solutions (synthetic Bayer liquors). Colloids and Surfaces **154**, 343–352

[58] Huàrez-Martìnez, G., Garza, C., Castillo, R. and Moreno, A. (2001) A dynamic light scattering investigation of the nucleation and growth of thaumatin crystals. Journal of Crystal Growth **232**, 119–131

[59] Malkin, A. J. and McPherson, A. (1994) Light-scattering investigations of nucleation processes and kinetics of crystallization of macromolecular systems. Acta Crystallographica D **50**, 385–395

[60] Wilson, W. W. (2003) Light scattering as a diagnostic for protein crystal growth - a practical approach. Journal of Structural Biology **142**, 56–65

[61] Gast, K., Damaschun, G., Misselwitz, R., and Zirwer, D. (1992) Application of dynamic light scattering to studies of protein folding kinetics. European Biophysical Journal **21**, 357–362

[62] Onuma, K., Oyane, A., Tsutsui, K., Tanaka, K., Treboux, G., Kanzaki, N. and Ito, A. (2000) Precipitation kinetics of hydroxyapatite revealed by the continuous-angle laser light-scattering technique. Journal of Physical Chemistry B**104**, 10563–10568

[63] Onuma, K. and Ito, A. (1998) Cluster growth model for hydroxyapatite. Chemistry of Materials **10**, 3346–3351

[64] Onuma, K., Kanzaki, N., and Kobayashi, N. (2004) Association of calcium phosphate and fibroblast growth factor-2: a dynamic light scattering study. Macromolecular Bioscience **4**, 39–46

[65] Pusey, P. N. in Linder, P. and Zemb, T., eds. *Neutron, X-Rays and Light: Scattering Methods Applied to Soft Condensed Matter* (Elseivier, Amsterdam, 2002)

[66] Berne, B.J. and Pecora, R. *Dynamic Light Scattering with applications to chemistry, biology and physics* (Dover Publications, New York, 2000).

[67] Spalla, O. in Linder, P. and Zemb, T., eds. *Neutron, X-Rays and Light: Scattering Methods Applied to Soft Condensed Matter* (Elseivier, Amsterdam, 2002)

[68] Glatter, O. in Linder, P. and Zemb, T., eds. *Neutron, X-Rays and Light: Scattering Methods Applied to Soft Condensed Matter* (Elseivier, Amsterdam, 2002)

[69] Chu, B. *Laser Light Scattering, basic principles and practice* (Academic Press, San Diego, 1991).

[70] Koppel, D. E. (1972) Analysis of macromolecular polydispersity in intensity correlation spectroscopy: the method of cumulants. Journal of Chemical Physics **57**, 4814–4820

[71] Gardel, M. L., Valentine, M. T., and Weitz, D. A. *Microscale Diagnostic Techniques* (Heidelberg, Springer—Verlag Berlin Heidelberg, 2005)

[72] Azzopardi, P. V. *Inhibition of hydroxyapatite growth by osteopontin phosphopeptides* M.Sc. Thesis (University of Western Ontario, London, 2009)

[73] Goldberg, H. A., Sodek, J. (1994) Purification of mineralized tissue-associated osteopontin. Journal of Tissue Culture Methods **16**, 211–215

[74] Hunter, G. K., Frohe, B., Jaffrey, S., O'Young, J., Sorensen, E. S., and Goldberg, H. A. (2008) Role of phosphate groups in inhibition of calcium oxalate crystal growth by osteopontin. Cells Tissues Organs **189**, 44–50

[75] Oyane, A., Onuma, K., Kokubo, T., and Ito, A. (1999) Clustering of calcium phosphate in the system $CaVl_2$-H_3PO_4-KCL-H_2O. Journal of Physical Chemistry B **103**, 8230–8235

[76] Jiang, H., Liu, X., Zhang, G., and Li, Y. (2005) Kinetics of template nucleation of self-assembled hydroxyapatite nanocrystallites by chondroitin sulfate. Journal of Biological Chemistry **280**, 42061–42066

[77] Goldsmith, H. L., Labrosse, J. M., McIntosh, F. A., Maenpaa P. H., Kaartinen, M. T. and McKee, M. D. (2002) Homotypic interactions of soluble and immobilized osteopontin. Annals of Biomedical Engineering **30** 840–850

[78] Beniash, E., Simmer, J. P., and Margolis, H. C. (903) The effect of recombinant mouse amelogenins on the formation and organization of hydroxyapatite crystals in vitro. Journal of Structural Biology **149**, 182–190

[79] Tsuji, T., Onuma, K., Yamamoto, A., Iijima, M., and Shiba, K. (2008) Direct transformation from amorphous to crystalline calcium phosphate facilitated by motif-programmed artificial proteins. Proceedings of the National Academy of Sciences **105**, 16866–6870

[80] Heiss, A., DuChesne, A., Denecke, B., Grotzinger, J., Yamamoto, K., Renne, T. and Jahnen-Dechent, W. (2003) Structural basis of calcification inhibition by α_2-HS glycoprotein/fetuin-A. Journal of Biological Chemistry **278**, 13333–13341

[81] Kanzaki, N., Treboux, G., Onuma, K., Tsutsumi, S., and Ito, A. (2001) Calcium phosphate clusters. Biomaterials **22**, 2921–2929

[82] Teng, S., Shi, J., and Chen, L. (2006) A novel method to synthesize large-sized hydroxyapatite rods. Journal of Crystal Growth **290**, 683–688

[83] Ito, A., Nakamura, S., Aoki, H., Akao, M., Teraoka, K., Tsutsumi, S., Onuma, K., and Tateishi, T. (1996) Hydrothermal growth of carbonate-containing hydroxyapatite single crystals. Journal of Crystal Growth **163**, 311–317

[84] Kanzaki, N., Onuma, K., Treboux, G., Tsutsumi, S., and Ito, A. (2001) Effect of impurity on two-dimensional nucleation kinetics: case studies of magnesium and zinc on hydroxyapatite (0001) face. Journal of Physical Chemistry B **105**, 1991–1994

[85] Tarasevich, B. J., Howard, C. J., Larson, J. L., Snead, M. L., Simmer, J. P., Paine, M., and Shaw, W. J. (2007) Journal of Crystal Growth **304**, 407–415